THE ASTROPHYSICAL JOURNAL, 443:152–168, 1995 April 10

THE NEUTRAL ATOMIC PHASES OF THE INTERSTELLAR MEDIUM

MARK G. WOLFIRE,[1] DAVID HOLLENBACH,[1] CHRISTOPHER F. MCKEE,[2]
A. G. G. M. TIELENS,[1] AND E. L. O. BAKES[3]
Received 1994 March 10; accepted 1994 October 21

ABSTRACT

We calculate the thermal equilibrium gas temperature of the diffuse interstellar medium. Our method incorporates a new photoelectric heating rate from small grains and PAHs that accounts for a size distribution of particles extending from 100 to 3 Å in radius. We also include a detailed treatment of the ionization rates and heating due to the soft X-ray background and due to cosmic rays. Phase diagrams (thermal pressure P versus hydrogen density n) are presented for gas that is illuminated by the local interstellar far-ultraviolet (FUV) and X-ray radiation fields. A stable two-phase medium is produced with thermal pressure in the range $P/k \simeq 10^3$–10^4 K cm^{-3}. We demonstrate that photoelectric heating from PAHs dominates in the warm neutral phase (WNM) and cold neutral phase (CNM). The WNM is cooled by Lyα, C II (158 μm), O I (63 μm), and electron recombinations onto positively charged grains. The CNM is cooled primarily by C II (158 μm). The C II (158 μm) cooling per hydrogen nucleus ranges from 2.6 to 6.6 $\times 10^{-26}$ ergs s^{-1} H^{-1} in the CNM and 0.31 to 0.81 $\times 10^{-26}$ ergs s^{-1} H^{-1} in the WNM, which compares favorably to recent observations. If the C II (158 μm) cooling per hydrogen nucleus in the solar neighborhood represents an average value for the Galaxy, we predict $L_{\rm C\,II} \simeq 7 \times 10^7\ L_\odot$ from the CNM in the Galaxy, comparable to that observed by *COBE*.

We discuss the dependence of the results on absorbing column density (10^{18} cm$^{-2} < N_w < 10^{20}$ cm^{-2}), gas-phase abundances (variations in C and O of $\sim$2), dust abundances and metallicity (from 0.003 to 3 times solar), FUV field (0.3–1000 times local values), and the X-ray radiation field (two models of background X-ray fluxes). These results will be useful in modeling the multiphase structure of high-velocity clouds in the halo, the ISM at other galactocentric radii, and the ISM in external galaxies and galactic nuclei.

Subject headings: dust, extinction — ISM: general

1. INTRODUCTION

Diffuse gas in the interstellar medium is observed to exist in three dominant phases: a cold ($T \gtrsim 50$ K) neutral medium (CNM), a warm ($T \sim 8000$ K) medium, both neutral (WNM; $n_e/n \sim 10^{-1}$) and ionized (WIM; $n_e/n \sim 1$), and a hot ($T \sim 10^6$ K) ionized medium (HIM) (McKee & Ostriker 1977, hereafter MO; see reviews by Kulkarni & Heiles 1987, 1988, and Spitzer 1990). The phases are observed in rough pressure equilibrium with $P/k \sim 10^3$–10^4 K cm^{-3} (Jenkins, Jura, & Loewenstein 1983; see also Kulkarni & Heiles 1987), although the dominant thermal and ionization processes in all phases are not well determined. This paper concentrates on the thermal and ionization balance of the atomic CNM and WNM phases and demonstrates the conditions under which a stable two-phase medium may exist in pressure equilibrium. In particular, we focus on the new photoelectric heating rates developed by Bakes & Tielens (1994) in which the heating process is derived at a fundamental level for a distribution of small grains and PAHs. In addition we also include a detailed calculation of the ionization fraction induced by the Galactic soft X-ray radiation field.

The thermal balance and stability of the CNM and the WNM has a long history of investigation. Field, Goldsmith, & Habing (1969) first showed that a two-phase medium can be maintained by cosmic-ray heating if the primary ionization rate is at least $\zeta_{\rm CR} \sim 4 \times 10^{-16}$ s^{-1}. Subsequent analysis, however, indicated that the cosmic ray ionization rate is significantly lower; a conclusion based on the small propagation distance of low-energy cosmic rays that dominate the ionization (Spitzer & Jenkins 1975), and the observations of several molecular species sensitive to the ionization rate (e.g., HD, Barsuhn & Walmsley 1977; OH, van Dishoeck & Black 1986; H_3^+, Black et al. 1990). In addition, a recent study by McKee (1994) finds a primary ionization rate in the WNM and CNM of $\zeta_{\rm CR} \sim 1.8 \times 10^{-17}$ s^{-1}, a rate which is a factor of at least 20 lower than needed to heat these phases.

Another potential heating source is the photoelectric ejection of electrons from dust grains by the interstellar radiation field (Watson 1972; Glassgold & Langer 1974; Jura 1976; Draine 1978; de Jong 1977, 1980). Ultraviolet photons can be absorbed by grains and dislodge internal electrons. Most of the electrons do not reach the surface, but a fraction, given by the photoelectric yield ($Y \sim 0.1$), are ultimately ejected from the grain. The energy consumed in liberating the electron includes collisional losses in the grain, and the energy required to overcome the work function and the Coulomb potential of accumulated positive grain charges. The remaining energy, typically $\sim$1 eV per ejected electron, is available for gas heating. Draine (1978) reexamined the photoelectric heating process introduced by previous authors. Using detailed physics of photoemission and using data based on laboratory measurements, he concluded that grains could heat the CNM but could not heat the WNM. De Jong (1977, 1980) adopted a parametric approach based upon the observed cooling in the diffuse interstellar medium (Pottasch, Wesselius, & van Duinen 1979). De Jong varied the grain properties, cosmic-ray ioniza-

[1] NASA Ames Research Center, MS 245-3, Moffett Field, CA 94035.
[2] Physics Department, and Astronomy Department, University of California at Berkeley, Berkeley, CA 94720.
[3] Princeton University, Peyton Hall, Princeton, NJ 08544.

tion rate, and gas-phase abundances until a reasonable two-phase medium was obtained.

In light of the low photoelectric heating found by Draine (1978), Ferrière, Zweibel, & Shull (1988) investigated the heating due to hydrodynamic wave dissipation. They concluded that wave heating is negligible in the CNM but could be an important source in the WNM. In addition, they found two phases for pressures in the range $P^{\min}/k \approx 130$ K cm$^{-3} \lesssim P/k \lesssim P^{\max}/k \approx 2000$ K cm^{-3}. However, these pressures are lower than observed in many regions of the Galactic plane. The data of Jenkins et al. (1983) and Jenkins & Shaya (1979) show that $\sim 56\%$ of the total column lies at a pressure greater than $P/k \gtrsim 2500$ K cm^{-3}; only about 14% of the observed total column of C I exhibits a pressure below $P/k = 1000$ K cm^{-3}. We also note that hydrodynamic wave heating diminishes with increasing ionization fraction. When ionization by cosmic rays (§ 2.2.2) and soft X-rays (§ 2.2.3) is included, the hydrodynamic heating rate at $P^{\max}$ derived by Ferrière et al. (1988) drops by a factor of ~ 2.

D'Hendecourt & Léger (1987) and Lepp & Dalgarno (1988) demonstrated that photoelectric emission from very small grains and large molecules (polycyclic aromatic hydrocarbons, or PAHs) could potentially be an important heating source. Verstraete et al. (1990) strengthened these arguments by using laboratory measurements of the photoionization cross sections for 2 PAH molecules to show that enhanced photoelectric heating by PAHs could produce two-phase media with $P^{\max} \lesssim 7400$ K cm^{-3}. Sutherland & Shull (1994) extended this analysis to include large grains, a population of small organic grains, and PAHs of a single mean size, and analyzed the relative contributions of the three components to the thermal pressure. Recently, Bakes & Tielens (1994, hereafter BT) presented a detailed discussion of the net heating produced by a distribution of particle sizes extending into the molecular domain. Their method incorporates the appropriate microphysics (ionization potential and photoelectric yield, for example) in all size regimes and includes a calculation of the expected charge distribution for each grain size. Compared to large grains, PAHs and very small grains have a greater photoelectric yield and smaller positive charge leading to a more efficient heating process.

In this paper we use the BT heating function. Thus, for the first time, we present a complete picture of the photoelectric heating and thermal instability in the diffuse interstellar medium using a realistic grain distribution and based entirely on the atomic physics. It is our intention to demonstrate that the model satisfies the observational constraints in the local interstellar medium and to provide quantitative predictions for the variation of all important parameters. The results are essential to understand the energy budget and volume filling factors, for example, of the various phases of diffuse gas in our Galaxy and in extragalactic systems, and they lay the foundation for future theoretical models in these areas.

We first discuss in § 2 the thermal and chemical processes included in our model. In § 3 we present phase diagrams for the interstellar medium and illustrate the dependence on the dominant model parameters. We compare our calculations with the results of previous investigators in § 4 and then apply our results to observations of the local interstellar medium, both in the plane and at high Galactic latitude. We also point out the possible applications of our results to the C II (158 μm) luminosity from the Galaxy as a whole, to high-velocity clouds in the Galactic halo, to different Galactic radii, and to starburst galaxies. The important points are summarized in § 5.

2. PHYSICAL PROCESSES

We calculate the equilibrium temperature T of a parcel of gas of density n that is exposed to the Galactic cosmic-ray flux and radiation field. We include the ionization and heating due to cosmic rays, soft X-rays, and far-ultraviolet (FUV) radiation. For all of the models presented in this paper the column of absorbing gas is restricted so that the gas is mainly atomic. For the CNM with $n \sim 100$ cm^{-3} and an unshielded dissociation rate of H_2 equal to 7.5×10^{-11} s^{-1} (Black & van Dishoeck 1987) this requires that $N(H^0) \lesssim 3 \times 10^{20}$ cm^{-2} for $2N(H_2)/N(H^0) = 0.1$ (Federman, Glassgold, & Kwan 1979).

We assume that the magnetic field does not lead to pressure differences between phases. For a static field, this will be true along field lines since a static field cannot exert a force parallel to itself. Alfvén waves can exert a force along the field (Dewar 1970), but we assume that the difference in wave pressures between different phases is negligible. The dominant thermal and chemical processes included in this study are listed in Table 1 and are discussed in more detail in the next three subsections.

2.1. *Abundances*

The total cooling in line radiation is sensitive to the gas-phase abundance of the coolants. We define $\mathscr{A}_i$ to be the gas phase abundance of element i relative to hydrogen, $\mathscr{A}_i = n_i/n$, where n is the density of hydrogen nuclei $n = n(H^+) + n(H^0) + 2n(H_2)$. A recent analysis of interstellar absorption lines toward ζ Oph, ξ Per, and δ Sco, using the *Hubble Space Telescope* (*HST*) indicates depletions of carbon by factors of ~ 1.4–2.7 (Cardelli et al. 1993). Theoretical models of the photodissociation region and H II region in Orion have shown that somewhat higher gas-phase abundances of C are needed to match the observed line emission from C I (370, 610 μm), C II (158 μm), and C III (1907 Å, 1909 Å) (Tielens & Hollenbach 1985b; Rubin, Dufour, & Walter 1993). We adopt a value of $\mathscr{A}_C = 3 \times 10^{-4}$, slightly less than solar abundance (3.63×10^{-4}; Anders & Grevesse 1989) and demonstrate in § 3.3 the effects of higher depletions.

The O abundance measured by Cunha & Lambert (1992) from stellar spectra in the Orion association is $\mathscr{A}_O = 4.6 \times 10^{-4}$, a factor of ~ 2 less than solar. Such a discrepancy between solar abundance and cosmic abundance could reflect self-enrichment of the molecular cloud which formed the Sun. In contrast, from observations of emission lines in the Orion Nebula, Walter, Dufour, & Hester (1992) argue that the oxygen abundance is closer to solar. For a standard model, we adopt the value from Cunha & Lambert (1992) for the gas-phase abundance, a value roughly consistent with the interstellar absorption line observations of Cardelli et al. (1993). In § 3.3, we investigate the dependence on different O abundances. For Si, S, and Fe we use gas-phase abundances from the compilations of Jenkins (1987) and Van Steenberg & Shull (1988), incorporating their fits to the variation of depletion with average density.

The heating and ionization rates due to soft X-rays depend on the elemental abundances. Depletion of the elements onto grains, as well as single or double ionization of elements heavier than He, affect the X-ray cross sections by less than 10%. We use the results of Anders & Grevesse (1989) to specify the abundances of all elements other than O. A summary of our adopted abundances, both elemental and gas phase, are given in Table 2.

TABLE 1

DOMINANT THERMAL AND IONIZATION PROCESSES (STANDARD MODEL)

Process	Notes	Reference
Photoelectric heating from small grains and PAHs		
FUV field	Draine field; $G_0 \approx 1.7$ in units of Habing field	1
Heating	$n\Gamma = 10^{-24} G_0 n\epsilon$ ergs cm^{-3} s^{-1}	2
	$\epsilon = 4.9 \times 10^{-2}[1.0 + 4.0 \times 10^{-3}(G_0 T^{1/2}/n_e)^{0.73}]^{-1} + 3.7 \times 10^{-2} (T/10^4)^{0.7}(1.0 + 2.0 \times 10^{-4} G_0 T^{1/2}/n_e)^{-1}$; n_e from ionization equilibrium	2
Ionization and heating by cosmic rays		
Primary ionization	$n\zeta_{CR} = 1.8 \times 10^{-17} n$ cm^{-3} s^{-1}	3
Secondary ionization	Primary $E = 35$ eV, n_e from ionization equilibrium	4
Heating	Primary $E = 35$ eV, n_e from ionization equilibrium	4
Ionization and heating by soft X-rays		
1. Unabsorbed component	$T_1 = 10^{6.16}$ K, EM$_1 = 5.3 \times 10^{-3}$ cm^{-6} pc, $N_1 = 0.0$ cm^{-2}	5, 6
2. Absorbed component	$T_2 = 10^{6.33}$ K, EM$_2 = 2.5 \times 10^{-3}$ cm^{-6} pc, $N_2 = 3.6 \times 10^{20}$ cm^{-2}	5, 6
3. Extragalactic component	$I_\nu \propto (h\nu)^{-0.4} e^{-\sigma N_3}$, $N_3 = 3.9 \times 10^{20}$ cm^{-2}	5, 6
Spectrum calculated for foreground absorption	Absorbing column $= N_w$	
Primary ionization	$n\zeta_{XR}$ from H, He, C, N, O, Ne, Mg, Si, S, Fe	7
Secondary ionization	From H and He, n_e from ionization equilibrium	4
Heating	n_e from ionization equilibrium	4
Recombinations		
Radiative recombination	H$^+$, He$^+$, C$^+$	8
Ion recombination on grains	H$^+$, He$^+$, C$^+$, neutralization, charge exchange, adsorption	9
Cooling by fine-structure lines		
C II	Impacts with H^0 and e^-, $\mathscr{A}_C = 3 \times 10^{-4}$	10, 11
O I	Impacts with H^0, e^-, and H$^+$, $\mathscr{A}_O = 4.6 \times 10^{-4}$	12
C I, Si I, Si II, S I, Fe I, Fe II	Minor coolants	8
Cooling by resonance lines		
Lyα	Important at $T \gtrsim 8000$ K	13
Cooling by metastable lines		
C I, C II, O I, O II, Si I, Si II, S I, S II, Fe I, Fe II	O I most important coolant	8
Cooling by recombination onto small grains and PAHs		
...	$n^2\Lambda = 4.65 \times 10^{-30} \eta n_e n$ ergs cm^{-3} s^{-1}	2
...	$\eta = T^{0.94}(G_0 T^{1/2}/n_e)^\beta$; $\beta = 0.735/T^{0.068}$; n_e from ionization equilibrium	

REFERENCES—(1) Draine 1978; (2) Bakes & Tielens 1994; (3) McKee 1994; (4) Shull & Van Steenberg 1985; (5) Garmire et al. 1992; (6) Raymond & Smith 1977, 1993; (7) Bałucińska-Church & McCammon 1992; (8) Hollenbach & McKee 1989; (9) Draine & Sutin 1987, eqs. (3.3), (3.4), and (5.9); (10) Launay & Roueff 1977; (11) Hayes & Nussbaumer 1984; (12) Péquignot 1990; (13) Spitzer 1978.

2.2. *Heating and Ionization*

2.2.1. *Photoelectric Heating from Small Grains and PAHs*

We use the results of BT to calculate the photoelectric heating. In their model, grains are distributed with a Mathis, Rumpl, & Nordsieck (1977, hereafter MRN) power-law distribution in size, $n(a)da \propto a^{-3.5} da$ between 3 and 100 Å in radius. Grains smaller than 15 Å are assumed to be disks while larger grains are assumed to be spheres (see BT). Since a range in particle sizes is included, the heating function is not dependent upon the properties of a single particular PAH species but instead is a result of the integrated properties from a range in sizes. With this distribution, species smaller than $\sim$15 Å ($\sim$4% of cosmic carbon) absorb about 10% of the total FUV flux. This is comparable to the observed ratio of the flux in the 3–10 μm emission features and plateaus to the total IR emission (Allamandola, Tielens, & Barker 1989). The remaining flux is absorbed by larger grains (mainly 15–300 Å). The smaller grains, however, have a much larger photoelectric efficiency and hence contribute about half of the photoelectric heating.

BT calculated the charge distribution for each particle size taking the photoionization and the electron and positive ion recombination into account and found the total photoelectric heating from the distribution of particles. The resulting heating rate is given by

$$n\Gamma = 1.0 \times 10^{-24} n\epsilon G_0 \text{ ergs cm}^{-3} \text{ s}^{-1}, \quad (1)$$

where ϵ is the fraction of FUV radiation absorbed by grains which is converted to gas heating (i.e., the heating efficiency) and G_0 is the incident FUV field normalized to Habing's (1968) estimate of the local interstellar value ($= 1.6 \times 10^{-3}$ ergs cm^{-2} s^{-1}). Dust extinction becomes important at a hydrogen column density $N \sim 1.2 \times 10^{21}$ cm^{-2}, but, since we are not considering columns this large, the FUV field is not attenuated by dust. BT provide a simple fit to ϵ as a function of

TABLE 2

ABUNDANCES

Element	Gas-phase Abundance[a]	Elemental Abundance[a]
He	-1.00	-1.00
C	-3.52	-3.44
O	-3.34	-3.34
Si	$-5.45-0.45 \times (\log n + 0.5)$	-4.45
Mg	$-4.84-0.28 \times (\log n + 0.5)$[b]	-4.41
Fe	$-6.15-0.38 \times (\log n + 0.5)$	-4.49
S	-5.10	-4.73
N[c]	...	-3.95
Ne[c]	...	-3.91

[a] Logarithmic number abundance relative to hydrogen, $\log_{10}(n_i/n)$.

[b] n_{Mg}/n is set at cosmic abundance ($\sim 3.98 \times 10^{-5}$) at densities $n \leq 8.5 \times 10^{-3}$ cm^{-3}.

[c] Element is included in ionization and heating by soft X-rays but not gas-phase cooling.

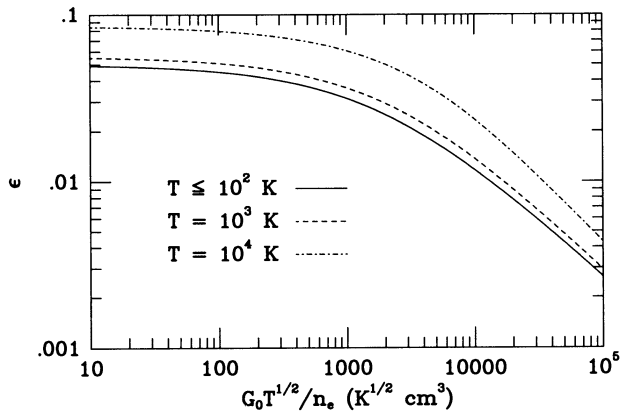

FIG. 1.—Photoelectric heating efficiency ϵ of small grains and PAHs (from Bakes & Tielens 1994) plotted as a function of $G_0\,T^{1/2}/n_e$. Curves are shown for gas temperatures $T \leq 10^2$ K (*solid*), $T = 10^3$ K (*dash*), $T = 10^4$ K (*dash-dot*). At small values of $G_0\,T^{1/2}/n_e$ ($\ll 5 \times 10^3$ K$^{1/2}$ cm^3) grains are mainly neutral and the efficiency is at a maximum. At larger values of $G_0\,T^{1/2}/n_e$ the efficiency drops due to grain charging.

$G_0\,T^{1/2}/n_e$:

$$\epsilon = \frac{4.9 \times 10^{-2}}{1.0 + [(G_0\,T^{1/2}/n_e)/1925]^{0.73}} + \frac{3.7 \times 10^{-2}(T/10^4)^{0.7}}{1.0 + [(G_0\,T^{1/2}/n_e)/5000]}, \quad (2)$$

where n_e is the electron density (see Fig. 1). The first term in equation (2) dominates the efficiency at low temperatures, with the second contributing $\sim 10\%$ at $T \sim 600$ K. The second term introduces an additional dependence on gas temperature which enhances the efficiency by a factor of ~ 1.7 at $T = 10^4$ K. This term is a result of the increase in the electron recombination rate onto grains at high temperatures, which lowers the grain (positive) charge and thereby increases the heating efficiency.

The combination $G_0\,T^{1/2}/n_e$ is proportional to the rate of ionization divided by the rate of recombination. At small values of $G_0\,T^{1/2}/n_e$ ($\ll 5 \times 10^3$ K$^{1/2}$ cm^3; eq. [2] and Fig. 1) grains are mainly neutral (or negatively charged) and the efficiency is at a maximum ($\epsilon \sim 0.05$–0.09 depending on the gas temperature). For all of the models discussed in this paper, $T < 1000$ K when $G_0\,T^{1/2}/n_e \ll 5 \times 10^3$ K$^{1/2}$ cm^3, so that the low-temperature value, $\epsilon \sim 0.05$, is appropriate (i.e., the first term in eq. [2] dominates at low values of $G_0\,T^{1/2}/n_e$). In this limit, the heating rate is regulated by the FUV field strength and grain density ($n\Gamma \propto nG_0$). Using equivalent radiation fields, the maximum heating rate is a factor of ~ 3 greater than that found by Draine (1978). At higher values of $G_0\,T^{1/2}/n_e$ the efficiency drops due to positive charging of the grains. The heating rate is then governed mainly by the electron recombination rate and the resulting grain charge. Higher rates of gas ionization due to cosmic rays or X-rays, for example, can increase the electron fraction in the gas and therefore increase grain photoelectric heating by decreasing the positive charge on the grains.

The photoelectric heating rate is fairly insensitive to the spectral energy distribution of the FUV radiation field. For the interstellar field, we use the energy distribution of Draine (1978). Keeping the integrated FUV flux constant, but changing the spectral shape to that of a 30,000 K blackbody (as for an FUV field dominated by distant O stars), decreases the heating efficiency by $\sim 25\%$. Equations (1) and (2) are normalized to the integrated field strength between 6 and 13.6 eV in units of G_0. We use $G_0 = 1.7$ for the local field, corresponding to the integrated Draine (1978) field. The photoelectric heating rate is also not very sensitive to the details of the grain size distribution, if they are maintained within observational constraints. We have adopted the MRN distribution extrapolated to the molecular domain which yields agreement with the observed 3–10 μm emission due to interstellar PAHs (Tielens 1993). Changing the shapes of grains smaller than 15 Å from disks to spheres decreases the heating rate by only $\sim 25\%$ (BT). However, the slope of the grain size distribution does affect the heating rate appreciably. Varying the grain size index from -3.5 to -4.5 leads to an increase in the heating by a factor of 3, but this would also result in a 3–10 μm flux which is three times larger than observed.

We note that the evolution of the grain size distribution in the ISM is not well determined (see reviews by Puget & Léger 1989 and Tielens 1993). Many processes have been proposed for the formation of PAHs including: injection into the ISM by C-rich stellar outflows (Keller 1987), shattering of large grains in shocks (Tielens & Allamandola 1987), and synthesis of PAHs from smaller hydrocarbons in diffuse gas through reactions of C^+ (Omont 1986) and in molecular clouds through ion-molecule and neutral reactions (Herbst 1991). Proposed destruction processes include sputtering in shocks (Jones et al. 1994), chemical reactions with H and O (Duley & Williams 1986), and photodestruction by UV photons (Puget, Léger, & Boulanger 1985). Since it is beyond the scope of this paper to resolve the important problem of the origin and evolution of interstellar PAHs, we assume that the grain distribution is the same in the CNM and WNM phases. Such an assumption is consistent with the recent observational results of Giard et al. (1994) who find a homogeneous mixing of PAHs in the diffuse ISM in the Galactic plane.

2.2.2. *Cosmic Rays*

We adopt a primary cosmic-ray ionization rate of $n\zeta_{CR} = 1.8 \times 10^{-17} n$ cm^{-3} s^{-1} (including the ionization of He) from the work of McKee (1994), who has updated the approach developed by Blandford & Ostriker (1980) and by Ip & Axford (1985). Cosmic rays are assumed to be injected with a power law in momentum, consistent with diffusive acceleration by shocks (e.g., Blandford & Eichler 1987). The steady state distribution of interstellar cosmic rays is determined by balancing injection with ionization losses and escape from the halo; the numerical values are set by requiring the resulting cosmic-ray spectrum to be consistent with observations in the solar system.

The total ionization rate, including secondary ionizations of H and He, is given by

$$n\xi_{CR} = n\zeta_{CR}[1 + \phi^{H}(E, n_e/n) + \phi^{He}(E, n_e/n)], \quad (3)$$

where the factors $\phi^{H}(E, n_e/n)$, and $\phi^{He}(E, n_e/n)$ give the number of secondary ionizations of hydrogen and helium produced per primary ionization. These functions depend on the primary electron energy E (with mean value approximately 35 eV; Spitzer 1978) and electron fraction n_e/n, and are taken from the Monte Carlo simulations of Shull & Van Steenberg (1985). Analytic expressions for ϕ^{H} and ϕ^{He} are given in Appendix A. Equation (3) yields a total ionization rate in diffuse clouds of $n\xi_{CR} = 3.0 \times 10^{-17} n$ cm^{-3} s^{-1}. This rate can be compared with the modeling results of van Dishoeck & Black (1986) for the ζ Per cloud. Using the "fast" dissociative recombination

rate for H_3^+ of $\sim 10^{-7}$ cm^3 s^{-1}, they find a cosmic-ray ionization rate (per hydrogen) of $n\zeta_{CR} \sim 5$–$10 \times 10^{-17} n$ cm^{-3} s^{-1} is needed to match the OH observations. Any OH formed in shocked or heated regions along the line of sight would reduce this estimate, although the fraction of shocked OH toward ζ Per is expected to be small.

The heating due to cosmic-ray ionizations is given by

$$n\Gamma_{CR} = n\zeta_{CR} E_h(E, n_e/n) , \quad (4)$$

where the function $E_h(E, n_e/n)$ gives the heat deposited for each primary electron of energy E (Shull & Van Steenberg 1985; Appendix A).

2.2.3. *Soft X-Rays*

The observed diffuse X-ray background arises from several different components (see review by McCammon & Sanders 1990). Extragalactic emission dominates at the highest energies (>10 keV) while emission at low energies ($\lesssim$0.25) keV is almost entirely Galactic. At intermediate energies, the background radiation is a mix of extragalactic and Galactic components, with contributions from the local bubble, Galactic disk, and halo.

The observed X-ray spectrum at energies $\gtrsim$0.1 keV has been fitted with a simple superposition of three separate components (e.g., Garmire et al. 1992; see Table 1). Component 1 consists of gas at a single temperature, T_1, and emission measure, EM_1, and can be interpreted as arising relatively nearby. Similarly, component 2 consists of a single temperature, T_2, and emission measure, EM_2, but with an intervening absorption layer of column N_2. This component can be interpreted as arising from hotter, more distant halo gas. The third component is extragalactic in origin and consists of a power-law emission spectrum [$\propto C_3(h\nu)^{-0.4}$] beyond an absorption layer N_3. Using the Garmire et al. (1992) parameters, we generate the spectrum for energies greater than 13.6 eV:

$$4\pi J_\nu = \tfrac{1}{2}[\Lambda_\nu(T_1)EM_1 + \Lambda_\nu(T_2)EM_2\, e^{-\sigma_\nu N_2} + C_3(h\nu)^{-0.4} e^{-\sigma_\nu N_3}] , \quad (5)$$

where $\Lambda_\nu(T)$ is the temperature-dependent emissivity from a Raymond & Smith (1977, 1993) plasma code, and σ_ν is the gas photoelectric absorption cross section per hydrogen taken from Bałucińska-Church & McCammon (1992). In calculating J_ν, we have conservatively assumed $4\pi J \approx 2\pi I$ as expected for radiation illuminating the surface of an opaque cloud or filament ($N \gtrsim 3 \times 10^{19}$ cm^{-2}). Since Garmire et al. (1992) adopted the elemental abundances of Allen (1976) in deriving the free parameters in equation (5) from the observations, we have similarly used these abundances in computing the X-ray spectrum (but have otherwise adopted the elemental abundance compilation of Anders & Grevesse [1989] as discussed in § 2.1).

Note that in calculating the X-ray spectrum we have neglected the contribution from discrete stellar sources. The EUV emission from hot (B) stars and hot white dwarfs is expected to be important in ionizing the WIM (MO), but will be absorbed in such a short column ($N \lesssim 10^{18}$ cm^{-2}) that it should not be important for the WNM. We also note that equilibrium models do not match in detail the recent spectral line results from the Diffuse X-Ray Spectrometer (Edgar et al. 1993; Sanders et al. 1993). Nevertheless, the parameter fit using the equilibrium models does provide a reasonable match to the broad-band emission.

The primary ionization rate of species i due to soft X-rays is given by

$$n\zeta^i_{XR} = 4\pi n \int \frac{J_\nu}{h\nu} e^{-\sigma_\nu N_w} \sigma^i_\nu d\nu \text{ cm}^{-3} \text{ s}^{-1} , \quad (6)$$

where the factor $e^{-\sigma_\nu N_w}$ accounts for an absorbing layer of warm material of column density N_w. We include the primary ionization of H, He I, He II, C, N, O, Fe, Ne, Mg, Si, and S, with photoelectric absorption cross sections, σ^i_ν per hydrogen, from Bałucińska-Church & McCammon (1992). The cross sections σ_ν and σ^i_ν incorporate the elemental abundances. The total ionization rate of H and He, including secondary ionizations, is given by

$$n\xi_{XR} = n\left[\zeta^H_{XR} + \sum_i \zeta^i_{XR}\langle\phi^H(E^i, n_e/n)\rangle\right] + n\left[\zeta^{He}_{XR} + \sum_i \zeta^i_{XR}\langle\phi^{He}(E^i, n_e/n)\rangle\right] \text{cm}^{-3} \text{ s}^{-1} , \quad (7)$$

where the factors $\langle\phi^H(E^i, n_e/n)\rangle$ and $\langle\phi^{He}(E^i, n_e/n)\rangle$ give the number of secondary ionizations per primary electron of energy E^i, averaged over the X-ray spectrum.

The heating rate is given by

$$n\Gamma_{XR} = 4\pi n \sum_i \int \frac{J_\nu}{h\nu} e^{-\sigma_\nu N_w} \sigma^i_\nu E_h(E^i, n_e/n) d\nu , \quad (8)$$

where the summation extends over species which suffer primary ionization. Our calculated rates of ionization and heating as a function of the (neutral) column N_w and ionization fraction n_e/n are presented in Figures 2*a* and 2*b*, respectively. We also provide simple parametric fits to these curves in Appendix A. Figure 2*a* shows that the ionization by soft X-rays dominates the cosmic-ray ionization for $N_w \lesssim 2 \times 10^{19}$ cm^{-2}.

It has been suggested that soft X-rays may be the dominant source of heating for the WNM (e.g., Silk & Werner 1969; Werner, Silk, & Rees 1970), depending on the distribution and strength of X-ray sources and the intervening absorption column. We shall demonstrate that the role of heating by soft X-rays is subordinate to that of FUV photoemission from grains, although the ionization by soft X-rays is essential for maintaining a high electron density and thereby controlling the grain photoelectric heating rate.

2.2.4. *Additional Heating and Ionization Processes*

In addition to ionization by X-rays and cosmic rays, we include for H and He the collisional impacts with H and e^- using rates from Hollenbach & McKee (1989, hereafter HM). The cooling due to these processes are also included. Species with ionization potential less than 13.6 eV (e.g., C I, Si I, Fe I) can be ionized by the FUV radiation field. The ionization of these species produces a minimum electron fraction of $n_e/n \sim 3 \times 10^{-4}$ at columns less than $N_w \lesssim 10^{21}$ cm^{-2}. We also include the heating due to photoionization of C I.

2.3. *Cooling and Recombination*

2.3.1. *Fine-Structure Lines*

Collisional excitation of the fine-structure lines of C II and O I is a dominant gas coolant at temperatures $T \lesssim 8000$ K. We include collisional impacts of C II with H^0 (Launay & Roueff 1977; Flower 1990) and e^- (Hayes & Nussbaumer 1984). For O I, we include H^0, e^-, and H^+ collisions from the compilation by Péquignot (1990). Additional cooling is provided by the

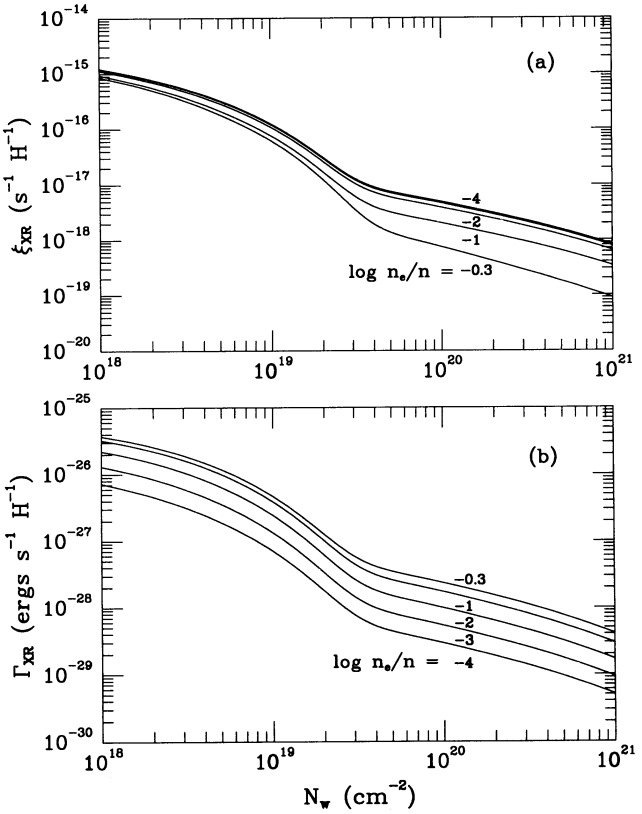

FIG. 2.—(*a*) Ionization rate per hydrogen ξ_{XR} due to the diffuse X-ray background. Secondary ionizations of H and He are included. (*b*) Heating rate per hydrogen Γ_{XR} due to the diffuse X-ray background. Curves are shown for electron fractions $n_e/n = 10^{-4}$, 10^{-3}, 10^{-2}, 10^{-1}, and 0.5 as a function of the neutral column N_w. Simple analytic fits are given in Appendix A.

fine-structure transitions of the ground electronic state of C I, Si I, Si II, S I, Fe I, and Fe II.

2.3.2. *Electron Recombination onto Positively Charged Grains*

Grains and PAHs may also be an important gas coolant. Net cooling results when the thermal energy of electrons ($\gtrsim kT$) recombining onto positively charged grains exceeds the energy of the ejected electron ($\lesssim 1$ eV; depending on the magnitude of the positive grain charge). This occurs at high temperatures, $T \gtrsim 10^4$ K, and for predominantly positively charged grains, $G_0\, T^{1/2}/n_e \gtrsim 5 \times 10^3$ K$^{1/2}$ cm^3. We treat the heating caused by the electron ejection (eq. [1]) and the recombination cooling separately, so that the net heating or cooling is the difference between the two. We use the fit to the recombination cooling provided by BT:

$$n^2\Lambda = 4.65 \times 10^{-30} T^{0.94} (G_0\, T^{1/2}/n_e)^{\beta} n_e n \text{ ergs cm}^{-3} \text{ s}^{-1}\,, \quad (9)$$

with $\beta = 0.74/T^{0.068}$.

2.3.3. *Resonance and Metastable Lines*

At the highest temperatures ($T \gtrsim 8000$ K) collisional excitation of H Lyα can contribute to the cooling. We also include low-lying metastable transitions of C I, C II, O I, O II, Si I, Si II, S I, S II, Fe I, and Fe II, using rates from HM.

2.3.4. *Additional Cooling and Recombination Processes*

The radiative recombination of H^+ is calculated using case B recombination rates. A fraction of the He^+ recombinations produce photons which can ionize H or He (e.g., Osterbrock 1989). Following HM we use the on-the-spot approximation for the recombination of He^+. Cooling due to inelastic collisions of neutral gas and grains are included (HM), although this process is found to be of negligible importance in the WNM and CNM phases.

Recombination of positive ions (H^+, He^+, C^+) on small grains can be important for the ionization balance when the recombination rate on grains exceeds the radiative rate. We use the Draine & Sutin (1987) formalism for ion-grain collisions along with the photoionization/photodetachment rates of BT to calculate the rates of ion neutralization with PAH^-, ion charge exchange with PAH^0, and ion adsorption on PAH^0. We assume that the coefficient for charge exchange and adsorption are equal with the sum given by the Draine & Sutin (1987) value for ion-neutral collisions. The rate coefficients are averaged over the disk population (3–15 Å). Larger grains (spheres) do not contribute significantly to the recombination rates due to their lower abundance and higher positive charge (see BT). We find that the recombination rates using several grain size bins vary by only $\sim 3\%$ from the average rates.

3. PHASE DIAGRAMS

The equations of thermal and ionization equilibrium at constant density n are solved numerically using an iterative process. We first select a gas temperature and solve for the species abundances in ionization equilibrium. A slightly modified version of the numerical code of Wolfire & Königl (1991) is used which solves for the equilibrium abundance, n_i, of 41 atomic and ionic species and includes charge exchange reactions. The network has been modified to include the additional ionization and recombination processes of § 2. We then check for thermal equilibrium ($n\Gamma = n^2\Lambda$) by calculating and comparing the summed heating and cooling rates. The temperature is increased or decreased accordingly and the cycle (chemistry followed by energy balance) is repeated until the temperature remains fixed to within 1%. Using this equilibrium temperature we construct phase diagrams by plotting the thermal pressure $P/k = T \sum_i n_i$ versus hydrogen density n, where the sum extends over all species (including electrons).

3.1. *The Standard Model*

We present in Figure 3*a* a phase diagram for an absorbing column of $N_w = 10^{19}$ cm^{-2}. Such a column density corresponds to a WNM cloud of mass of about 1 $M_\odot$. Substantially smaller columns correspond to negligible cloud mass and thus cannot be typical. Substantially larger columns ($N_w \sim 10^{20}$ cm^{-2}, for example) correspond to WNM cloud diameters $\gtrsim 100$ pc, much larger than would be expected in a three-phase ISM (MO). We shall adopt $N_w \sim 10^{19}$ cm^{-2} as the standard value and consider $N_w \sim 10^{18}$ cm^{-2} and $N_w \sim 10^{20}$ cm^{-2} for particular cases.

Field (1965) discussed the criteria for stability of gas in thermal equilibrium (see also reviews by Shull 1987, and Begelman 1990). In a plot of P/k versus n, regions of thermal stability occur for $d(\log P)/d(\log n) > 0$. Thus, Figure 3*a* shows that a stable two-phase medium, corresponding to the WNM and CNM, can be maintained in pressure equilibrium for P/k between $P^{\min}/k \simeq 990$ K cm^{-3} and $P^{\max}/k \simeq 3600$ K cm^{-3}. For pressures less than $P^{\min}$, only the warm phase is possible, while at pressures greater than $P^{\max}$ only the cold phase is possible. We list in Table 3 the allowed range in pressure for a two-phase medium along with the corresponding range in

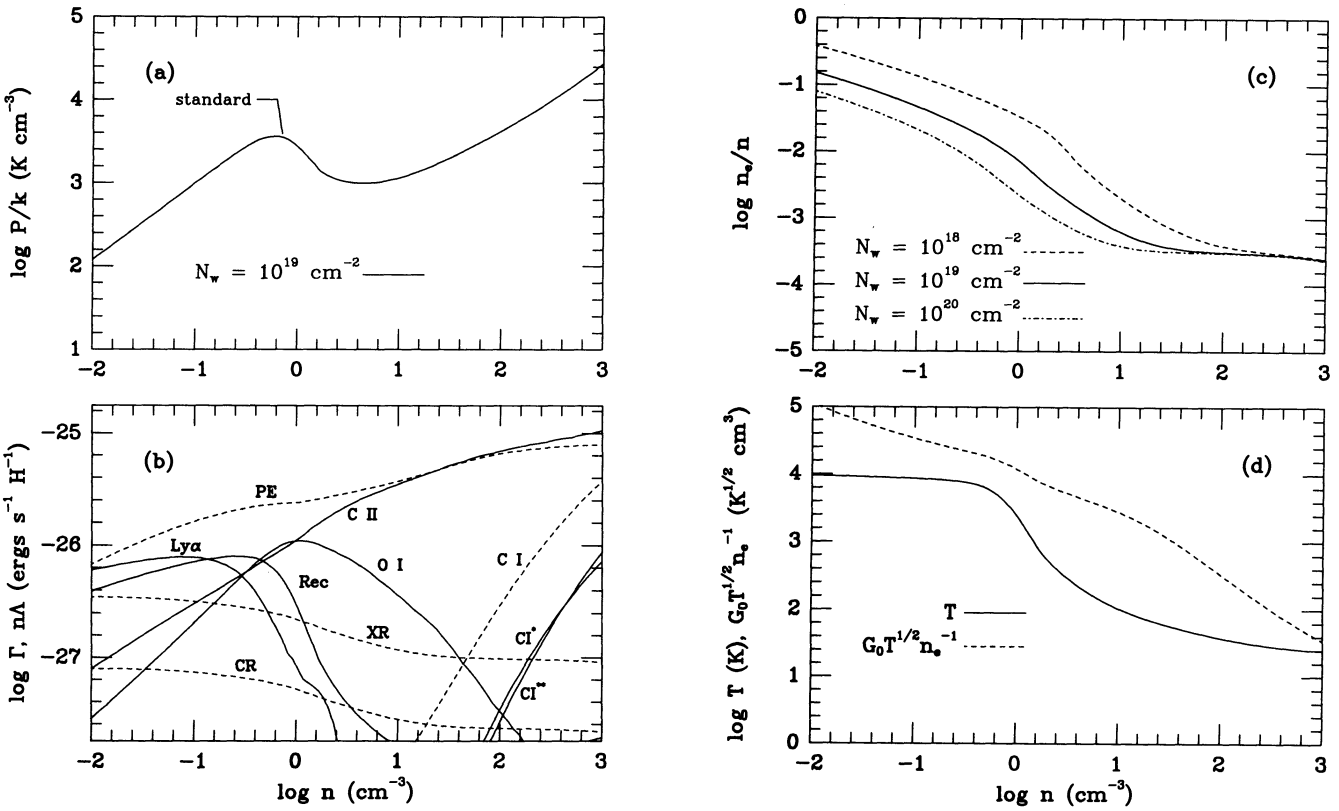

FIG. 3.—(*a*) Thermal pressure P/k vs. hydrogen density n for standard model (see § 3.1). Gas is thermally stable for $d(\log P)/d(\log n) > 0$. (*b*) Heating and cooling rates per hydrogen nucleus vs. density n for pressure curve of panel *a*. Heating rates (*dash*); Photoelectric heating from small grains and PAHs (PE); X-ray (XR); Cosmic ray (CR); photoionization of C (C I). Cooling rates (*solid*); C II fine-structure (C II); O I fine-structure (O I); Recombination onto small grains and PAHs (Rec); Lyα plus metastable transitions (Lyα); C I fine-structure 609 μm (C I*); C I fine-structure 370 μm (C I**). (*c*) Electron fraction n_e/n as a function of hydrogen density n for the pressure curve of panel *a* (*solid*). Also shown are curves for $N_w = 10^{18}$ cm^{-2} (*dash*), and $N_w = 10^{20}$ cm^{-2} (*dash-dot*). (*d*) Gas temperature T (*solid*) and ionization parameter $G_0 T^{1/2}/n_e$ (*dash*) as a function of hydrogen density n for the pressure curve of panel *a*.

density and temperature for each phase. At an equilibrium pressure of $P/k = 3000$ K cm^{-3} we find for the standard case a WNM with $T = 7300$ K, $n = 0.37$ cm^{-3}, and $n_e/n = 1.9 \times 10^{-2}$, and a CNM with $T = 45$ K, $n = 61$ cm^{-3}, and $n_e/n = 3.3 \times 10^{-4}$.

Figure 3*b* shows the separate heating and cooling processes per hydrogen for the thermal equilibrium curve shown in Fig. 3*a*. Photoelectric emission from small grains and PAHs dominates the heating at all densities $n > 10^{-2}$ cm^{-3}. Heating from soft X-rays contribute less than ~35% to the total at $n = 10^{-2}$ cm^{-3} and less than ~1% at $n = 10^3$ cm^{-3}. The decline in X-ray and cosmic-ray heating at high densities is due to the decreasing electron fraction (see also Fig. 3*c*) which channels the primary electron energy into ionization and excitation rather than heat.

Cooling at densities $n \lesssim 0.1$ cm^{-3} ($T \gtrsim 7000$ K) is partly due to electron recombination onto positively charged grains and partly due to radiative loses from hydrogen Lyα and metastable transitions of O I. The fine-structure lines dominate at $n \gtrsim 1$ cm^{-3} ($T \lesssim 2300$ K) with comparable C II and O I cooling. The O I cooling drops at higher densities (corresponding to lower temperatures) due to the Boltzmann factor $\propto e^{-228/T}$ and due to the temperature dependence of the collisional rate coefficients, leaving C II as the dominant coolant. The excitation of the fine-structure levels is in the low-density limit for most of the parameter space considered here. For O I (63 μm) the critical densities for collisional de-excitation (at $T = 300$ K) at $n_{cr}^{H} \approx 2 \times 10^5$ cm^{-3}, $n_{cr}^{e} \approx 1 \times 10^5$ cm^{-3}, and $n_{cr}^{p} \approx 1 \times 10^5$ cm^{-3} for impacts with neutral hydrogen, electrons, and protons respectively, while for C II, $n_{cr}^{H} \approx 3 \times 10^3$ cm^{-3} and $n_{cr}^{e} \approx 10$ cm^{-3}. Thus, (at constant electron fraction) the cooling per unit volume behaves as $n^2\Lambda \propto n^2$.

We show in Figure 3*c* the run of the electron fraction n_e/n as a function of n and in Figure 3*d* the run of T and $G_0 T^{1/2}/n_e$. The contribution to the electron fraction by soft X-ray ionization balanced by radiative recombination scales approximately as $n_e/n \propto n^{-1/2}$ with a somewhat steeper drop with density near $n \sim 1$ cm^{-3} due to a sharply decreasing gas temperature that increases the rate coefficient for H^+ recombination. Ion recombination on grains becomes comparable to radiative recombination at densities greater than ~0.3 cm^{-3} ($n_e/n \lesssim 0.03$), thereby reducing the electron abundance obtained from the radiative rates alone. The reduction in n_e reaches a maximum (about a factor of 3 drop) near $n \sim 10$ cm^{-3}. At high density, the ionization of C due to FUV radiation produces a minimum electron fraction of $n_e/n \sim 3 \times 10^{-4}$.

The thermal instability is a consequence of the density and temperature dependence of the various cooling processes. At low densities ($n \lesssim 0.1$ cm^{-3}), the fine-structure line cooling by C II and O I is insignificant, and the temperature rises to ~10^4 K, where the strong temperature dependence of the Lyα and recombination cooling thermostats the temperature. As density is raised, the cooling by C II and O I eventually dominates. This occurs in our standard model at $n \gtrsim 0.5$ cm^{-3}.

TABLE 3

MODEL RESULTS: RANGE OF PHYSICAL CONDITIONS FOR TWO-PHASE MEDIUM

		WNM			CNM			
PARAMETER[a]	$P^{min} - P^{max}$ (K cm^{-3})	T (K)	n (cm^{-3})	n_e/n	T (K)	n (cm^{-3})	n_e/n	FIGURE
(Standard)[b,c]	990–3600	8700 –5500	0.10–0.59	0.046–0.013	210–41	4.2–80	1.3(−3)[d]–3.2(−4)	3*a–d*
$N_w = 10^{18}$ cm^{-2}	1600–1.0(4)	9200 –5600	0.15–1.6	0.11–0.023	160–30	9.2–310	2.2(−3) –3.1(−4)	4
$N_w = 10^{20}$ cm^{-2}	610–1500	8200 –4900	0.064–0.28	0.029–0.0093	240–65	2.4–20	9.3(−4) –3.3(−4)	4
$\mathscr{A}_C = 3.0(-5)$	2900–6500	8500 –5400	0.31–1.1	0.022–0.0075	420–110	6.3–55	9.2(−4) –1.0(−4)	5
$\mathscr{A}_C = 1.5(-4)$ $\mathscr{A}_O = 3.0(-4)$	2100–7200	8800 –6000	0.21–1.1	0.029–0.0077	210–47	9.2–140	6.2(−4) –1.6(−4)	5
$\mathscr{A}_C = 1.5(-4)$	1700–5000	8600 –6100	0.18–0.73	0.032–0.011	310–54	5.2–87	1.1(−3) –1.8(−4)	5
$\mathscr{A}_O = 7.9\,(-4)$	810–2300	8400 –4900	0.086–0.41	0.051–0.016	310–52	2.4–40	2.2(−3) –3.5(−4)	5
$D/G = 3.0$	3300–9300	9500 –6400	0.31–1.3	0.014–0.0038	330–57	9.2–150	5.3(−4) –2.9(−4)	6*a*
$D/G = 0.3$	200–800	8600 –4600	0.020–0.15	0.11–0.027	170–40	1.1–18	4.8(−3) –5.6(−4)	6*a*
$D/G = 0.1$	61–370	9000[e]–5500	0.0050[e]–0.058	0.22[e]–0.064	140–33	0.41–10	8.2(−3) –9.8(−4)	6*a*
$D/G = 0.03$	34–280	9000[e]–5100	0.0025[e]–0.048	0.30[e]–0.069	110–26	0.28–10	9.5(−3) –1.1(−3)	6*a*
$D/G = 0.01$	29–270	9000[e]–5800	0.0020[e]–0.039	0.34[e]–0.078	110–23	0.23–11	1.1(−2) –4.4(−3)	6*a*
$D/G = 0.003$	27–260	9000[e]–5600	0.0018[e]–0.039	0.37[e]–0.077	110–23	0.23–10	1.0(−2) –1.1(−3)	6*a*
$Z = D/G = 3.0$	900–2300	8600 –5000	0.095–0.41	0.036–0.011	340–52	2.6–40	1.8(−3) –9.2(−4)	6*b*
$Z = D/G = 0.3$	1300–6500	8500 –5400	0.14–1.1	0.047–0.012	150–31	7.6–190	1.1(−3) –1.1(−4)	6*b*
$Z = D/G = 0.1$	1800–1.3(4)	8400 –5900	0.19–1.9	0.042–0.011	150–26	11–460	1.2(−3) –5.0(−5)	6*b*
$Z = D/G = 0.03$	3400–3.0(4)	8200 –6400	0.37–4.2	0.031–0.0084	130–24[e]	25–1200[e]	8.7(−4) –3.5(−5)[e]	6*b*
$Z = D/G = 0.01$	7200–7.1(4)	7900 –5700	0.81–11	0.022–0.0052	100–20[e]	65–3300[e]	5.3(−4) –3.2(−5)[e]	6*b*
ISRF × 0.3[f]	390–1900	9000 –5100	0.039–0.34	0.070–0.015	150–32	2.4–54	1.4(−3) –3.1(−4)	7
ISRF × 0.5[f]	580–2500	8800 –5600	0.058–0.41	0.059–0.015	180–35	2.9–65	1.4(−3) –3.2(−4)	7
ISRF × 3[f]	2300–6300	8400 –5300	0.25–1.1	0.031–0.010	220–54	9.2–110	9.9(−4) –3.3(−4)	7
ISRF × 10[f]	5400–1.2(4)	8000 –4500	0.60–2.4	0.021–0.0073	300–82	17–140	9.5(−4) –3.3(−4)	7
ISRF × 10^2[f]	2.6(4)–3.6(4)	5700 –2900	4.2–11	0.034–0.0037	530–200	44–170	9.9(−4) –4.1(−4)	7
MO,[g] $N_w = 10^{18}$ cm^{-2}	1330–6100	8900 –6100	0.13–0.89	0.070–0.018	180–33	6.3–170	1.6(−3) –3.1(−4)	…[h]
MO,[g] $N_w = 10^{19}$ cm^{-2}	850–2600	8500 –4700	0.086–0.50	0.038–0.0093	220–48	3.5–49	1.1(−3) –3.2(−4)	…[h]
MO,[g] $N_w = 10^{20}$ cm^{-2}	610–1500	8100 –4900	0.067–0.28	0.028–0.0093	240–65	2.4–20	9.4(−4) –3.3(−4)	…[h]
$X_0 = 0.1$	990[i]–3100[i]	8300 –4600	0.10[j]–0.60[j]	0.045–0.012	210–43	4.2[j]–65[j]	1.3(−3) –3.3(−4)	8
$X_0 = 10$	1000[i]–3800[i]	8800 –5700	0.10[j]–0.60[j]	0.046–0.012	220–50	4.2[j]–69[j]	1.3(−3) –3.2(−4)	8
$X_0 = 10^2$	1500[i]–4200[i]	8700 –5200	0.13[j]–0.73[j]	0.040–0.011	320–120	4.2[j]–32[j]	1.4(−3) –3.8(−4)	8
$X_0 = 10^3$	3400[i]–6200[i]	8200 –5200	0.37[j]–1.1[j]	0.019–0.0076	720–230	4.2[j]–25[j]	1.7(−3) –4.4(−4)	8

[a] Modified parameter. All additional parameters held fixed at their standard values.

[b] Standard model parameters: $N_w = 10^{19}$ cm^{-2}; $\mathscr{A}_C = 3 \times 10^{-4}$; $\mathscr{A}_O = 4.6 \times 10^{-4}$; $G_0 = 1.7$; Garmire et al. (1992) soft X-ray spectrum; $D/G = 1$; $Z = 1$; $X_0 = 1$; see also Tables 1 and 2.

[c] Physical conditions for standard model at typical pressure $P/k = 2300$ (K cm^{-3}): WNM $T = 8000$ K, $n = 0.26$ cm^{-3}, $n_e/n = 2.5 \times 10^{-2}$; CNM $T = 53$ K, $n = 41$ cm^{-3}, $n_e/n = 3.4 \times 10^{-3}$.

[d] The notation a(−b) means a × 10^{-b}.

[e] Estimated from Fig. 6.

[f] FUV field strength in units of interstellar radiation field.

[g] Soft X-ray spectrum calculated from McKee & Ostriker 1977 parameters.

[h] Pressure curve not shown.

[i] Pressure scaled by X_0; P/kX_0.

[j] Density scaled by X_0; n/X_0.

Cooling by C II then results in a rapid drop in gas temperature and an unstable region in the phase diagram. As the temperature drops below the energy spacing of the C II (158 μm) transition ($\Delta E/k = 92$ K), the temperature decline becomes more gradual, thereby leading to a rise in pressure in the stable CNM region.

The dependence of the photoelectric heating per hydrogen Γ on n is somewhat complex. We note that as n_e increases (with increasing n; Fig. 3*c*) photoelectric heating rises due to the decreased charge of the grains and PAHs (Figs. 1 and 3*d*). At values of $G_0\,T^{1/2}/n_e \ll 5000$ K$^{1/2}$ cm^3, the grains are mainly neutral, and heating reaches the maximum efficiency so that Γ becomes only weakly dependent on density. In addition, the temperature dependence of ϵ introduces an indirect density dependence as well. Thus, the combined dependence on density flattens from $\Gamma \propto n^{0.4}$ at low density ($n \lesssim 0.1$ cm^{-3}) to $\Gamma \propto n^{0.1}$ at higher density ($n \gtrsim 10$ cm^{-3}), as shown in Figure 3*b*. For our standard model (Fig. 3), the density dependence of Γ is seen to change, first, near $n \sim 1$ cm^{-3}, due to a rapid drop in temperature (ϵ dependence), and second, near $n \gtrsim 3$ cm^{-3}, where the value of $G_0\,T^{1/2}/n_e$ drops below 5000 K$^{1/2}$ cm^3. As a result of this reduced heating, the C II cooling dominates over Lyα and recombinations at a lower value of n than would otherwise be the case if the heating continued to rise with a 0.4 power of density. Hence, the thermal instability results from the temperature and density dependence of the cooling, especially the C II cooling. However, the density at which the instability is initiated is influenced by the temperature and density dependence of heating.

We have tested the effects of hydrodynamic wave heating by including the heating rate from Ferrière et al. (1988). Using our calculated ion abundances for the ion-neutral collision rate, we find that wave heating increases the pressure by only ~5% at P^{max}.

A basic assumption of our treatment is that the gas is in thermal and ionization balance. In reality, the ISM is highly time dependent; for example, the three-phase model of the ISM predicts that the typical time interval between significant

pressure fluctuations is about 4×10^5 yr (MO). These pressure fluctuations are transmitted directly to clouds sufficiently small that this time exceeds the sound crossing time (radii less than about 4 pc for warm clouds, or 0.4 pc for cold clouds); larger clouds tend to average these fluctuations out. For a gas in thermal balance, the thermal timescale is equal to both the heating time and the cooling time. Under isobaric conditions, the former is

$$t_{\rm heat} = \frac{(5/2)(1.1 + x_e)kT}{\Gamma} = 1.2 \times 10^5 \left(\frac{T}{100\ {\rm K}}\right)\left(\frac{10^{-26}\ {\rm ergs\ s^{-1}\ H^{-1}}}{\Gamma}\right)\ {\rm yr}\ , \quad (10)$$

provided the ionization $x_e = n_e/n$ is negligible. Our results (see § 4) show that the heating rate per hydrogen is typically $\Gamma \simeq 6 \times 10^{-26}$ ergs s^{-1} H^{-1} in the CNM and 2×10^{-26} ergs s^{-1} H^{-1} in the WNM. As a result, the thermal timescale in the CNM is quite short, $\sim 2 \times 10^4$ yr, and the assumption that the gas is in thermal balance is quite good for this phase. However, for the warm gas the thermal timescale is about 100 times longer, and as a result the WNM is not necessarily in thermal balance. Consideration of the ionization and recombination timescales leads to the same conclusion: the CNM is generally in ionization balance, whereas the WNM may not be. Nonetheless, an analysis of two-phase *equilibria* remains valuable because, for pressures at which a WNM equilibrium exists, the conditions in the WNM will inevitably evolve toward the equilibrium; the equilibrium conditions thus represent an average of the conditions to be expected in the actual WNM.

Finally, we note that the thermal instability can also be analyzed using the criteria developed by Field (1965). We have carried out this analysis and confirmed that the combined heating and cooling processes satisfy the Field instability criterion for isobaric perturbations.

3.2. *Dependence on Column Density*

As seen in Figure 2, the heating and ionization due to soft X-rays is sensitive to the absorbing column, N_w. In this subsection we demonstrate the effects of different values of N_w. Figure 4 shows the variation in the pressure curve with $N_w = 10^{18}$ cm^{-2}, 10^{19} cm^{-2}, and 10^{20} cm^{-2}. At $N_w = 10^{18}$ cm^{-2} the peak pressure is higher than for the $N_w = 10^{19}$ cm^{-2} case. The enhanced ionization of H and He by X-rays increases the electron density in the gas which leads to more efficient photoelectric heating from grains. In addition, the X-rays contribute as much as $\sim 30\%$ to the total heating at the peak pressure. The ionization and heating due to soft X-rays are close to their maximum values for $N_w = 10^{18}$ cm^{-2} (Fig. 2), so that pressure curves are unchanged for $N_w \lesssim 10^{18}$ cm^{-2}.

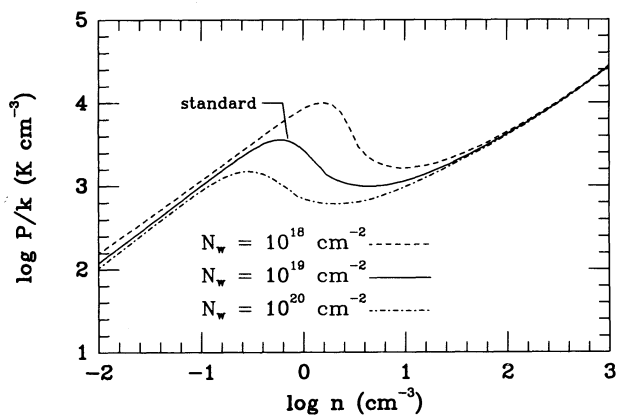

FIG. 4.—Thermal pressure P/k for various absorbing columns N_w. Curves are shown for P/k vs. hydrogen density n for $N_w = 10^{18}$ cm^{-2} (*dash*), $N_w = 10^{19}$ cm^{-2} (*solid*), and $N_w = 10^{20}$ cm^{-2} (*dash-dot*).

For $N_w = 10^{20}$ cm^{-2}, both $P^{\rm min}$ and $P^{\rm max}$ drop below their values for $N_w = 10^{19}$ cm^{-2} due to the diminished X-ray heating and ionization. A critical rate of ionization is set by the cosmic-ray ionization rate. When the ionization rate by soft X-rays is much less than $\xi_{\rm CR}$, then the electron fraction (and the rate of photoelectric heating) is set by cosmic-ray ionization. We find that for $N_w \gtrsim 3 \times 10^{19}$ cm^{-2}, the X-ray ionization rate is less than half of the cosmic-ray ionization rate; as a result the photoelectric heating is only $\sim 10\%$ higher than the level set by cosmic-ray ionization acting alone. At larger columns, the pressure curves remain unchanged until dust extinction reduces the FUV field, at $N_w \gtrsim 10^{21}$ cm^{-2}. The allowed range in pressure for each column along with the range in n and T are summarized in Table 3.

We also show in Figure 3*c* the electron fraction, n_e/n versus density for the absorption columns $N_w = 10^{18}$ cm^{-2}, 10^{19} cm^{-2}, and 10^{20} cm^{-2}. At the lowest columns, and at low density, ionization is dominated by soft X-rays, with $\xi_{\rm XR} \sim 50\xi_{\rm CR}$. As the density increases, radiative recombination and ion recombination on grains results in a lower electron fraction. At the highest densities the electron fraction approaches the limit set by FUV ionization of C ($n_e/n \sim 3 \times 10^{-4}$). In contrast, at the *highest* columns, and lowest densities, ionization is dominated by cosmic rays with $\xi_{\rm CR} \sim 10\xi_{\rm XR}$, and with n_e/n similarly approaching the FUV limit at high densities.

3.3. *Dependence on Gas Phase Abundances*

We have adopted nearly undepleted gas-phase abundances of C and O. In this subsection we illustrate the effects of higher depletions, and a larger elemental O abundance. Figure 5 shows the variation in pressure with gas-phase C and O abundances of ($\mathscr{A}_{\rm C} = 3.0 \times 10^{-5}$, $\mathscr{A}_{\rm O} = 4.6 \times 10^{-4}$), ($\mathscr{A}_{\rm C} = 1.5 \times 10^{-4}$, $\mathscr{A}_{\rm O} = 4.6 \times 10^{-4}$), and ($\mathscr{A}_{\rm C} = 1.5 \times 10^{-4}$, $\mathscr{A}_{\rm O} = 3.0 \times 10^{-4}$); the first two sets represent a decrease in the gas-phase carbon abundance by factors of 10 and 2, and the third set represents a decrease of carbon by 2 and oxygen by 1.5. The P/k curves, along with $P^{\rm min}/k$ and $P^{\rm max}/k$, rise with decreasing abundances. The effect is largest at the high densities, where cooling is dominated by fine-structure line emission. We note that for the case of high C depletion the two phase medium is still possible, but in a very restricted range of pressures. In this case, oxygen dominates the cooling and is responsible for the region of thermal instability. Also shown in Figure 5 is the effect of increasing the oxygen abundance to a value of $\mathscr{A}_{\rm O} = 7.9 \times 10^{-4}$ (Walter et al. 1992), which is nearly solar abundance. The increased fine-structure line cooling from O I (63 μm) lowers the pressure curve slightly between $n \sim 0.3$ and ~ 10 cm^{-3} (see summary of $P^{\rm max}$, $P^{\rm min}$, n, and T in Table 3).

3.4. *Dependence on Metallicity*

In the previous subsection we discussed the variation in the gas-phase abundance of C and O. Here we illustrate the effects of varying the dust-to-gas ratio D/G (dust abundance), and the metallicity, Z (elemental abundances). We normalize so that $D/G = 1$ and $Z = 1$ correspond to our standard model. We assume that a drop in metallicity results in decreased abun-

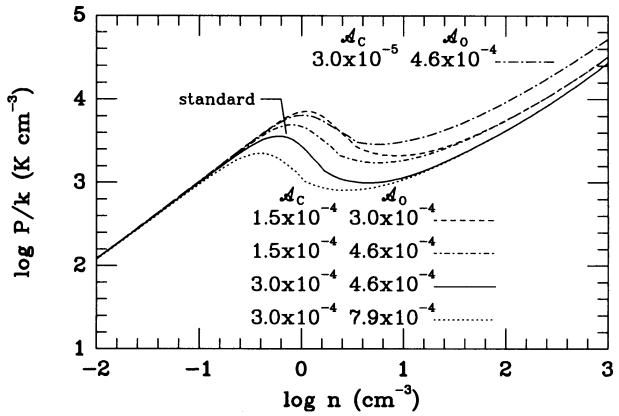

FIG. 5.—Thermal pressure P/k for various gas phase abundances. Curves are shown for P/k vs. hydrogen density n for an absorbing column of $N_w = 10^{19}$ cm^{-2} and abundances $\mathscr{A}_C = 3.0 \times 10^{-5}$, $\mathscr{A}_O = 4.6 \times 10^{-4}$ (*long dash-dot*); $\mathscr{A}_C = 1.5 \times 10^{-4}$, $\mathscr{A}_O = 3.0 \times 10^{-4}$ (*dash*); $\mathscr{A}_C = 1.5 \times 10^{-4}$, $\mathscr{A}_C = 4.6 \times 10^{-4}$ (*dash-dot*); $\mathscr{A}_C = 3.0 \times 10^{-4}$, $\mathscr{A}_O = 4.6 \times 10^{-4}$ (*solid*); and $\mathscr{A}_C = 3.0 \times 10^{-4}$, $\mathscr{A}_O = 7.9 \times 10^{-4}$ (*dot*).

dances of all elements (with the exception of H and He), and grains by the same fraction (i.e., $Z = D/G$). A reduction in Z, as may occur within the Galaxy with distance from the center and with height above the plane, causes a drop in the grain photoelectric heating and gas cooling, and at large values of $N_w \gtrsim 10^{19}$ cm^{-2}, can also lead to decreased ionization and heating by soft X-rays. The grain abundance can be further reduced by grain destruction, for example in interstellar shocks of speed $v_s \gtrsim 100$ km s^{-1}, with only a minor enhancement in gas phase abundances of C and O (Jones et al. 1994). In this case $D/G \lesssim Z$, and a reduction in D/G directly reduces the photoelectric heating rate.

Figure 6*a* shows a phase diagram for decreasing dust abundances while holding the gas-phase metal abundances fixed. Curves are shown for a range of dust-to-gas ratios spanning $D/G = 3$ to $D/G = 0.003$ times the BT abundance. As photoelectric heating diminishes, X-ray heating becomes more important. The pressure curves are unchanged for $D/G \lesssim 0.01$, where the X-ray and cosmic-ray heating dominates and photoelectric heating is of negligible importance. At these low values of D/G, two phases are possible for 25 K cm$^{-3} \lesssim P/k \lesssim 250$ K cm^{-3}. For $D/G = 3$, the rise in heating due to an increased grain abundance is partially offset by a drop in heating efficiency resulting from ion recombinations on grains which lowers n_e.

Figure 6*b* shows a phase diagram for simultaneously varying the dust abundance and metallicity (with $Z = D/G$). Here a drop in photoelectric heating is initially offset by a lower abundance of gas coolants. However, as photoelectric heating drops below X-ray heating, the diminished cooling results in higher temperatures and pressures. For $Z = D/G \gtrsim 1$, ion recombinations on grains lowers n_e leading to a drop in the heating efficiency and a reduction in pressure.

3.5. *Dependence on FUV Field*

Figure 7 shows the variation in pressure with FUV radiation field, spanning a range between 0.3 times the interstellar field ($G_0 = 0.51$) to 10^3 times the interstellar field ($G_0 = 1.7 \times 10^3$); see also Table 3. The FUV field strength will increase independently of the cosmic-ray flux or soft X-ray flux in regions close to OB associations. For example, the field illuminating the reflection nebula NGC 7023 is estimated to be $G_0 \sim 3 \times 10^3$ (Chokshi et al. 1988).

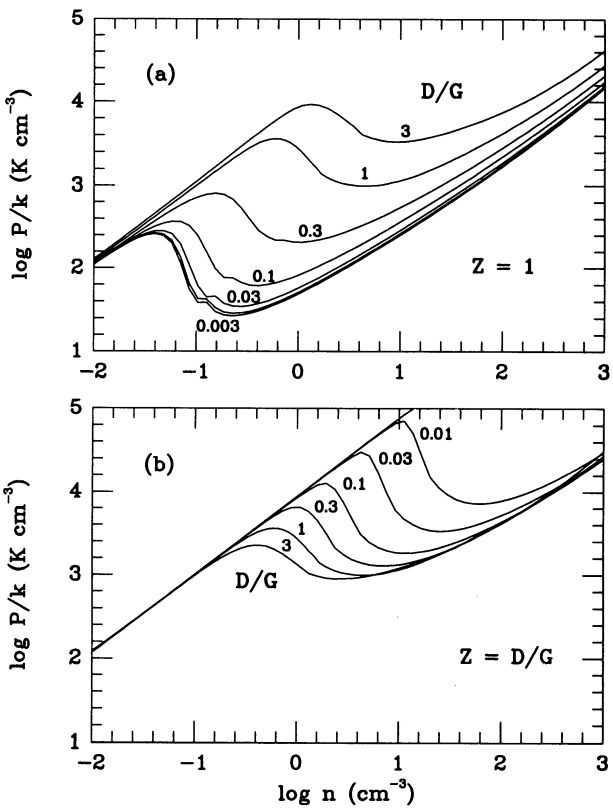

FIG. 6.—Thermal pressure P/k of various dust-to-gas ratios, D/G, and metallicities Z. Curves are shown for P/k vs. hydrogen density n for a range of D/G and Z relative to local interstellar values. (*a*) Variable D/G with fixed $Z = 1$. (*b*) Variable D/G and Z with $Z = D/G$.

At low values of G_0 ($0.3 \lesssim G_0 \lesssim 3$), the temperature of the WNM is determined by the balance between photoelectric heating in the high-temperature limit $G_0 T^{1/2}/n_e \gg 5 \times 10^3$ K$^{1/2}$ cm^3, and gas radiative cooling (atomic resonance and metastable transitions), while for the CNM the temperature is determined by the balance between photoelectric heating in the low-temperature limit $G_0 T^{1/2}/n_e \ll 5 \times 10^3$ K$^{1/2}$ cm^3 and C II fine-structure cooling. The emerging dominance (with

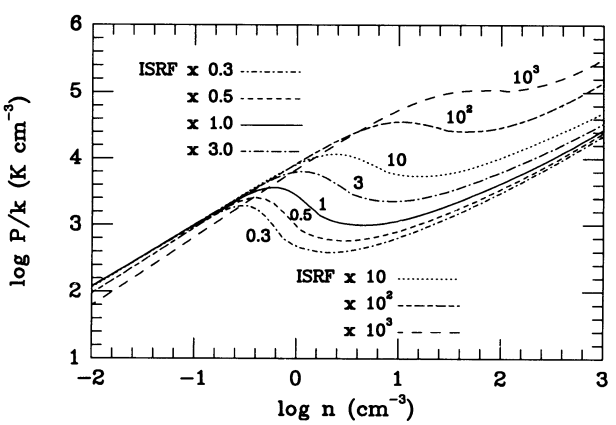

FIG. 7.—Thermal pressure P/k for various FUV field strengths. Curves are shown for P/k vs. hydrogen density n for an absorbing column of $N_w = 10^{19}$ cm^{-2} and a Draine (1978) interstellar FUV radiation field, (ISRF; corresponding to $G_0 = 1.7$) $\times 0.3$ (*dash-dot*), $\times 0.5$ (*dash*), $\times 1$ (*solid*), $\times 3$ (*long dash-dot*), $\times 10$ (*dot*), $\times 10^2$ (*short dash-long dash*), and $\times 10^3$ (*long dash*).

increasing n) of the fine-structure line cooling over the resonance and metastable transitions causes the temperature to decline at P^{max}. As G_0 rises, P^{max} occurs at increasingly higher densities. This is because the photoelectric heating rises with G_0, and thus higher densities are required for C II to dominate the cooling.

At higher FUV field strength ($G_0 > 3$) the effects of grain recombination cooling and O I fine-structure cooling become important. For $G_0 T^{1/2}/n_e \gg 5 \times 10^3$ K$^{1/2}$ cm^3 the gas temperature is determined by the balance between photoelectric heating and grain recombination cooling

$$T \approx 8000\left[\left(\frac{n_e}{10^{-2}\ \mathrm{cm}^{-3}}\right)\left(\frac{10^2}{G_0}\right)\right]^{0.086}\ \mathrm{K}\,. \qquad (11)$$

Since in this limit the temperature is nearly independent of density (with $n_e \propto n^{1/2}$ we have $T \propto n^{0.04}$), the pressure curve rises nearly linearly with n, along a line of constant temperature. As G_0 rises, grain charging leads to enhanced recombination cooling and slightly lower gas temperatures and pressures. Similar to the low-G_0 case, the thermal instability occurs at the density at which the strong line cooling (O I and C II) dominates recombination cooling which causes the temperature to rapidly fall.

Since photoelectric heating and recombination cooling are both fairly insensitive to the gas temperature, uncertainties in the total heating or cooling rate can have large effects on the calculated temperature in the limit where equation (11) applies. We note that for the average ISM ($G_0 \approx 1$) at low density ($n \lesssim 0.1$ cm^{-3}), radiative cooling by Lyα always dominates over recombination cooling. Therefore, the temperature enters exponentially in the cooling rate, and hence the calculated temperature is much less sensitive to these uncertainties.

As seen in Figure 7, for $G_0 \lesssim 10^2$, P^{min} and P^{max} both rise with G_0 due to the enhanced photoelectric heating (see also Table 3). However, P^{min} rises faster than P^{max}, so that for $G_0 > 10^2$ only one stable phase is possible at a single pressure. The rapid rise in P^{min} is the result of the temperature dependence of the fine-structure line cooling. In particular, the O I (63 μm) cooling, which becomes increasingly important in the high G_0 models, has a strong temperature dependence in both the collision rate coefficient and Boltzmann factor. As was seen in § 3.3, this temperature dependence reduces the difference between P^{min} and P^{max}. In addition, P^{max} is suppressed owing to the increased effect of recombination cooling. The combination of these two effects eliminate the unstable region for $G_0 > 10^2$.

We note that the low C abundance model presented in § 3.3 ($G_0 = 1.7$, $\mathscr{A}_C = 3.0 \times 10^{-5}$) shows a weak two-phase structure even with the cooling at P^{max} dominated by O I (63 μm) emission. In that case, however, the temperature at low densities was not reduced by strong recombination cooling, and the temperature drop due to O I alone was sufficient to create an unstable region.

3.6. *Dependence on X-Ray Radiation Field*

In previous sections we have used a soft X-ray radiation field based on the three-component fit to the observed (local) spectrum by Garmire et al. (1992). The observed spectrum may be unusual since the Sun lies inside a large $\sim$100 pc "bubble" of hot gas. Here we compare model results in which we replace the local component (emission part 1 discussed in § 2.2.3) with a theoretically derived spectrum while retaining emission components 2 and 3. The spectrum is calculated using the prescription given in MO for the intensity from a smooth distribution of emitting gas and a clumpy distribution of absorbing clouds. This may represent a field more typical of that seen from an average location in the Galactic plane.

We find that at energies less than $\sim$0.1 keV, the flux drops below that of the local component of Garmire et al. (1992) due to the large opacity at these energies and the relatively short mean free path between cloud envelopes. (We note that the Garmire et al. [1992] fits use data from energies greater than 0.1 keV.) As a result, the peak pressure for $N_w = 10^{18}$ cm^{-2} is $\sim$40% less than for the Garmire et al. (1992) spectrum. At columns $N_w \gtrsim 2 \times 10^{19}$ cm^{-2} the two radiation fields produce similar curves since the ionization and heating becomes dominated by the halo and extragalactic components.

4. DISCUSSION

4.1. *Comparison with Previous Work*

We compare, in Table 4, the results of our standard model (§ 3.1) with those of several previous investigators. Listed are the minimum and maximum pressures for a two-phase medium, along with the corresponding range in temperatures and densities for the WNM and CNM phases. Models that rely predominantly on cosmic-ray heating (Field et al. 1969), hydrodynamic wave heating (Ferrière et al. 1988), or photoelectric heating from large grains (Draine 1978; Shull & Woods 1985), all produce low ($<$2200 K cm^{-3}) peak pressures. The semi-empirical de Jong (1977, 1980) photoelectric heating model shows pressures and densities similar to our standard case. The Verstraete et al. (1990) models, which also include the photoelectric heating from PAHs, produce peak pressures somewhat higher than our results.

The Verstraete et al. (1990) models differ in several key aspects from our calculations. Verstraete et al. (1990) carried out their analysis with essentially a single sized (planar) particle consisting of 80 carbon atoms ($\sim$8 Å in radius). This PAH could either be neutral, in which case it contributes to the

TABLE 4

COMPARISON WITH PREVIOUS WORK

		WNM		CNM	
REFERENCE	$P^{min}/k - P^{max}/k$ (K cm^{-3})	T (K)	n (cm^{-3})	T (K)	n (cm^{-3})
This work	990–3600	8700–5500	0.10–0.59	210–41	4.2–80
de Jong 1980	2900–5000	7000–4600	0.38–1.0	240–69	11–66
Ferrière et al. 1988	130–2200	20000–8000	0.0057–0.25	98–20	1.2–60
Field et al. 1969	90–1800	10000–7500	0.0082–0.22	82–17	1.0–100
Shull & Woods 1985	70–260	7200–3800	0.0089–0.063	290–87	0.22–2.7
Verstraete et al. 1990	3700–7400	6400–4000	0.52–1.7	150–45	23–150

heating, or singly ionized, in which case it does not contribute to the heating since they assumed the second ionization potential to be $\gtrsim 13.6$ eV. The total PAH abundance was found by assuming that PAHs of this size account for 10% of the cosmic carbon abundance. In contrast, BT included a size distribution of particles with a calculation of the charge distribution for each size. Half of the photoelectric heating arises from grains smaller than $N_C \sim 1500$ carbon atoms (grain radius $a \sim 15$ Å) containing $\sim 4\%$ of the cosmic carbon abundance. The remaining heating is produced by larger ($N_C \sim 1500$–5×10^5, $a \sim 100$ Å), more highly charged grains.

There are also significant differences in the fine-structure line cooling. Verstraete et al. (1990) use gas-phase C and O abundances that are $\sim 30\%$ lower than those used in our standard model. In addition they use a collision strength for e impacts on C II which is up to a factor of ~ 2 lower than used here. Together these differences in the heating and cooling processes tend to drive temperatures upward in the Verstraete et al. (1990) models.

4.2. *Application to Local ISM*

Our local ISM models listed in Table 3 ($G_0 = 1.7$, standard abundances, and 10^{19} cm$^{-2} \leq N_w \leq 10^{20}$ cm^{-2}) show a range of possible pressures (610 K cm$^{-3} \leq P/k \leq 3600$ K cm^{-3}) for a two-phase equilibrium corresponding to a range of temperatures (40 K $\lesssim T \lesssim$ 240 K) for the CNM and (4900 K $\lesssim T \lesssim$ 8700 K) for the WNM. Kulkarni & Heiles (1987) reviewed the available temperature data for these phases. They tentatively conclude that the WNM temperature lies in the range 6000 K $\lesssim T \lesssim 10^4$ K based on the 21 cm line width (Mebold 1972), and optical depth (e.g., Mebold et al. 1982; Payne, Salpeter, & Terzian 1983), and the UV absorption measurements of various ions (e.g., York & Frisch 1984). The 21 cm absorption measurements in the CNM indicate temperatures ranging from ~ 20 to ~ 250 K over column densities of $\sim 2 \times 10^{20}$–3×10^{19} cm^{-2} (Payne et al. 1983). We conclude that our calculations agree well with the observations, although we do not produce a simple $T-\tau$ relation in the CNM as observed by Lazareff (1975) and Payne et al. (1983). There is some indication that the CNM temperatures derived from observations increases with decreasing 21 cm optical depth. In contrast, our calculated temperatures are independent of optical depth except in a very narrow range of pressures near $P^{\min}$ (see Fig. 4 and Table 3). Further observational and theoretical investigation of this relation is warranted.

The calculated pressures for a two-phase medium agree with those observed by Jenkins et al. (1983). We note that our value of $P^{\min}$ drops below 1000 K cm^{-3} for FUV field strengths less than the average interstellar field. In particular, for a field strength equal to one-half the interstellar average ($G_0 = 0.85$), we find $P^{\min}/k \approx 580$ K cm^{-3}. Thus, the small fraction of gas observed at pressures less than 1000 K cm^{-3} could correspond to clouds illuminated by an FUV field slightly lower than the average value.

The heating in the local diffuse interstellar medium has been derived by Pottasch et al. (1979) and by Gry, Lequeux, & Boulanger (1992) from observations of the UV line absorption of C^+ in the $^2P_{3/2}$ level and the hydrogen column density. These observations yield the average cooling rate in the $^2P_{3/2} \rightarrow {}^2P_{1/2}$ transition per hydrogen nucleus. If C II dominates the cooling, as it does in the CNM, and if thermal equilibrium holds, this measurement gives an estimate of the energy input. Pottasch et al. (1979) concluded that the heating rate was remarkably constant over a range of cloud conditions with an average value of $\sim 10^{-25}$ ergs s^{-1} H^{-1} (i.e., per hydrogen nucleus). Gry et al. (1992) found a wider range in values with an average ($\sim 3.5^{+5.4}_{-2.1} \times 10^{-26}$ ergs s^{-1} H^{-1}), somewhat lower than that of Pottasch et al. (1979). However, the cooling rates found by Pottasch et al. (1979) are probably biased toward high values, since at least some of the clouds in their sample are illuminated by FUV radiation fields greater than the interstellar average. For example, van Dishoeck & Black (1986) determined that an incident FUV field strength of $G_0 \approx 5$ is appropriate for the line of sight toward ζ Oph. Our models then predict a photoelectric heating rate of $\sim 2 \times 10^{-25}$ ergs s^{-1} H^{-1} (eqs. [1]–[2]), which compares well with the observed value of 1.0×10^{-25} ergs s^{-1} H^{-1} from Pottasch et al. (1979). Furthermore, the Gry et al. (1992) observations are necessarily biased toward low column densities where the UV absorption is not saturated. Consequently, their lowest cooling rates appear to be lines of sight in which the column is mostly WNM, which we find to have a C II cooling rate which is nearly a factor of ~ 10 lower than the CNM. Our standard model shows a nearly constant rate of $\sim 6.2 \times 10^{-26}$ ergs s^{-1} H^{-1} for the CNM and $\sim 6.2 \times 10^{-27}$ ergs s^{-1} H^{-1} for the WNM. We conclude that our calculated cooling rates are consistent with the observed rates when we account for the high-FUV fields associated with the Pottasch et al. (1979) observations and the low column densities inherent in the Gry et al. (1992) observations.

We list in Table 5 the calculated cooling rates per hydrogen nucleus for C II in the CNM and WNM, and for O I fine-structure emission, grain recombination, and Lyα plus metastable transitions, in the WNM (the latter cooling processes are expected to be of minor importance in the CNM for $G_0 \lesssim 3$). We also include in Table 5 the expected C II cooling in the WIM from Appendix B. At a pressure of $P/k = 3000$ K cm^{-3} and the interstellar radiation field ($G_0 = 1.7$), the ratio of emissivities per hydrogen nucleus are $n\Lambda_{\rm C\,II}^{\rm CNM}:n\Lambda_{\rm C\,II}^{\rm WIM}:n\Lambda_{\rm C\,II}^{\rm WNM}:n\Lambda_{\rm O\,I}^{\rm WNM}:n\Lambda_{\rm Rec}^{\rm WNM}:n\Lambda_{\rm Ly\alpha}^{\rm WNM} = 1.0{:}1.3{:}0.10{:}0.10{:}0.13{:}0.071$, with $n\Lambda_{\rm C\,II}^{\rm CNM} = 6.2 \times 10^{-26}$ ergs s^{-1} H^{-1}. We have also provided in Appendix B an analytic expression for $n\Lambda_{\rm C\,II}$ as a function of $n_{\rm H^0}$, n_e, and T.

One need be extremely cautious about applying these local results to the Galaxy as a whole. However, if the local conditions represent a Galactic average, then a mass of 2.5×10^9 $M_\odot$ in CNM, would yield a total luminosity in the C II (158 μm) line comparable to the 5×10^7 $L_\odot$ observed by *COBE* (Wright et al. 1991); we note that Kulkarni & Heiles (1987) cite a total H I mass (CNM + WNM) for the Galaxy of 3.5×10^9 $M_\odot$. Since there is much less mass in WIM than CNM, the C II luminosity from WIM is less significant. We shall examine the dependence of our results on galactocentric radius in a future paper.

As seen in Figure 3, temperatures are much higher in the WNM phase than in the CNM phase, although the energy input into the WNM, $\Gamma \approx 2.5 \times 10^{-26}$ ergs s^{-1} H^{-1}, is less than that in the CNM, $\Gamma \approx 6.2 \times 10^{-26}$ ergs s^{-1} H^{-1}. Lower electron densities in the WNM lead to grain charging and less efficient photoelectric heating. However, the lower densities in the WNM also lead to less cooling and thus elevated temperatures ~ 5500–8600 K (Table 3). We find that in the WNM phase, the cooling by the C II (158 μm) line is comparable to the cooling in the Lyα and O I (63 μm) transitions and to the cooling by electron recombinations onto positively charged grains (Fig. 3*b* and Table 5). Thus a measure of the C II line

TABLE 5

COOLING RATES PER HYDROGEN NUCLEUS[a]

G_0[b]	(P/k)[c]	$\log_{10} N_w$[d]	$n\Lambda_{C\,II}^{CNM}$	$n\Lambda_{C\,II}^{WIM}$[e]	$n\Lambda_{C\,II}^{WNM}$	$n\Lambda_{O\,I}^{WNM}$	$n\Lambda_{Rec}^{WNM}$	$n\Lambda_{Ly\alpha}^{WNM}$
5.1.....	4000	19	11	10.8	0.80	0.81	1.5	0.75
1.7.....	3000	19	6.2	8.1	0.62	0.64	0.78	0.44
1.7.....	2000	19	5.1	5.4	0.46	0.41	0.79	0.66
1.7.....	1000	19	2.8	2.7	0.31	0.21	0.71	0.78
0.85.....	2000	19	3.5	5.4	0.44	0.41	0.53	0.41
0.85.....	1000	19	2.7	2.7	0.29	0.21	0.50	0.63
0.51.....	1000	19	2.1	2.7	0.29	0.22	0.39	0.49
1.7.....	4000	18	7.9	10.8	1.5	0.86	1.9	3.3
1.7.....	3000	18	7.4	8.1	1.3	0.64	1.8	3.6
1.7.....	2000	18	6.8	5.4	1.0	0.44	1.7	3.9
0.85.....	3000	18	4.8	8.1	1.3	0.65	1.3	2.7
0.85.....	2000	18	4.6	5.4	0.98	0.43	1.2	3.1
0.85.....	1000	18	4.3	2.7	0.64	0.23	1.0	3.5
1.7.....	1000	20	3.0	2.7	0.21	0.22	0.40	0.17

[a] Calculated cooling rate in units 10^{-26} ergs s^{-1} H^{-1} for C II 158 μm, O I 63 μm, electron recombination onto positively charged grains, and Lyα plus metastable transitions.

[b] FUV field strength G_0 in units of Habing (1968) field. A Draine 1978 interstellar field corresponds to $G_0 = 1.7$.

[c] Thermal pressure of interstellar medium in units K cm^{-3}.

[d] Absorbing column N_w in units cm^{-2}.

[e] C II cooling in the WIM is calculated from eq. (B6).

intensity underestimates the total heating in the WNM by a factor of $\sim$3–4.

Several recent observations have been conducted of the C II cooling rate at high Galactic latitude. Bock et al. (1993) measured directly the C II (158 μm) line emission along several lines of sight. They estimate the cooling rate to be between 1.2 and 3.3×10^{-26} ergs s^{-1} (H I-atom)$^{-1}$ (i.e., per neutral hydrogen), with a best-fit value of $2.6 \pm 0.6 \times 10^{-26}$ ergs s^{-1} (H I-atom)$^{-1}$. Savage et al. (1993) report *HST* observations toward 3C 273 of the UV absorption from $C^+ {}^2P_{3/2}$. Using the observed column of S II to find the total column of hydrogen, Savage et al. (1993) find a cooling rate $\sim 1.4 \times 10^{-26}$ ergs s^{-1} H^{-1}. In addition, Spitzer & Fitzpatrick (1993) present *HST* observations toward the high-latitude star HD 93521. They distinguish nine components along the line of sight, and provide the columns of $C^+ {}^2P_{3/2}$ and S^+ for each. From their data we derive a C II cooling of ~ 3.8–4.6×10^{-26} ergs s^{-1} H^{-1} in the four lowest velocity components (heliocentric $v \geq -18.2$ km s^{-1}). The cooling in the higher velocity (and presumably more distant) components are all somewhat lower and span a range of values (0.58–2.0×10^{-26} ergs s^{-1} H^{-1}), with an average value of $\sim 1.2 \times 10^{-26}$ ergs s^{-1} H^{-1}. Thus, the cooling rates measured at high Galactic latitude are quite a bit lower than the average values found by Pottasch et al. (1979) and Gry et al. (1992) for the cooling along nearby lines of sight in the Galactic plane. However, observations at high latitude are expected to sample lower values of G_0, lower thermal pressures, and, due to the local bubble, lower columns of CNM than for lines of sight in the plane. We thus expect a lower cooling rate from C II in these directions. This is consistent with the conclusions of Savage et al. (1993) that the line of sight toward 3C 273 samples mainly the low-density gas, based on the observed low average density (~ 0.05 cm^{-3} to a height of 1 kpc), and the modest depletions of Mn, Si, and Ni.

We can calculate the expected C II cooling rate for a line of sight passing through the halo. The average columns of CNM and WNM are estimated from the observations of Kulkarni & Fich (1985) toward the North Galactic Pole: $N(H^0) \simeq 1.54 \times 10^{20}$ csc $|b|$ cm^{-2} and $N^{CNM} \simeq 0.39 \times 10^{20}$ csc $|b|$ cm^{-2}. The neutral hydrogen that is not cold is presumably in the WNM, but a portion is in the WIM. For an electron column density $N_e = 7 \times 10^{19}$ csc $|b|$ cm^{-2} (Reynolds 1991a), and an ionization of 0.85 (Mathis 1986), the total column density of the WIM is $N^{WIM} = 0.82 \times 10^{20}$ csc $|b|$ cm^{-2}. Subtracting the neutral component of the WIM from $N(H^0)$ leaves a column density $N^{WNM} = 1.03 \times 10^{20}$ csc $|b|$ cm^{-2} in the WNM. These column densities can be combined with the emissivities from Table 5 to yield the average C II cooling per hydrogen nucleus along a line of sight:

$$\langle n\Lambda_{C\,II} \rangle = \frac{N^{CNM}(n\Lambda_{C\,II}^{CNM}) + N^{WNM}(n\Lambda_{C\,II}^{WNM}) + N^{WIM}(n\Lambda_{C\,II}^{WIM})}{N^{CNM} + N^{WNM} + N^{WIM}}. \quad (12)$$

The C II cooling per neutral H^0 is a factor of ~ 1.4 higher. Thus, for $G_0 = 0.85$ (0.5 times the disk value, allowing for the reduced solid angle for FUV irradiation) and for $P/k \simeq 2000$ K cm^{-3} as estimated for a line of sight through the Galactic halo (Appendix B), we predict $\langle n\Lambda_{C\,II} \rangle \approx 2.8 \times 10^{-26}$ ergs s^{-1} H^{-1}. The fraction of the total C II line intensity from each phase along a line of sight through the halo is then $f^{CNM} \approx 0.22$, $f^{WNM} \approx 0.07$, $f^{WIM} \approx 0.71$. We emphasize that the dominance of the WIM in the halo is directly caused by the large ratio of N^{WIM}/N^{CNM}, and is not the case for the Galaxy as a whole.

Using this model, our calculated values are within a factor of 1.5 (higher) of the Bock et al. (1993) observations and within a factor of 2 (higher) of the Savage et al. (1993) observations. There are several possible means of accounting for these discrepancies. Perhaps the most likely is that our estimates are based on observations which average over the entire sky at $b > 45°$, whereas the observations of Bock et al. (1993) and Savage et al. (1993) refer to particular lines of sight. There are large fluctuations in the WIM; for example, the Hα intensity toward the H I hole in Ursa Major—part of the field studied by Bock et al. (1993)—is less than 20% of the value expected from Reynolds's (1992) global fit (Jahoda, Lockman, & McCammon 1990). Alternatively, the depletion of carbon could be greater than we have assumed; reducing the gas-phase carbon abun-

dance by a factor of 2 brings the C II cooling rate within a few percent of the Savage et al. (1993) observations. Finally, if the temperature (and hence the pressure) of the WIM is less than we have assumed, then the predicted C II cooling rate is reduced: at a temperature of 5000 K, the pressure in the WIM is somewhat less than 1000 K cm^{-3} (see Appendix B) and the predicted cooling rate is 2.2×10^{-26} ergs s^{-1} H^{-1} (for our standard carbon abundance).

In this section we have compared our theoretical results with observations of the local ISM in the plane and toward high Galactic latitude. We find that the standard model matches reasonably well the range of temperatures of the diffuse ISM derived from 21 cm observations, the pressures determined from C I absorption, and the cooling rates determined from C II emission. However, the model predictions differ from observations along particular lines of sight, especially at high latitude, by up to a factor of 2, which we ascribe to variations in local conditions, such as the incident FUV field, pressure, elemental depletion, and the relative columns of WNM, WIM, and CNM.

4.3. *Application to Nonlocal ISM and Extragalactic Systems*

The model results presented in § 3.1 use parameters appropriate for local Galactic conditions. Values for the FUV field strength, G_0, the soft X-ray flux, and the cosmic-ray ionization rate, ξ_{CR}, vary in more distant regions or in extragalactic systems. These ionization and heating processes are all related to a single source: the formation and subsequent supernova explosions of massive stars. Therefore, G_0, the soft X-ray flux, and ξ_{CR} should globally scale together with the rate of massive star formation or, equivalently, the supernova rate.

When cosmic-ray heating dominates, phase diagrams obey a common scaling law when plotted as $(P/k\zeta)$ versus (n/ζ), where ζ is the cosmic-ray ionization rate (Dalgarno & McCray 1972). In Figure 8 we show a phase diagram for P/kX_0 versus n/X_0 where, X_0 is the common multiplier for G_0, ξ_{CR}, and the soft X-ray flux. A value of $X_0 = 1$ means that parameters take on the values given by our standard model. Curves are shown for $X_0 = 0.1$, 1, 10, 100, and 10^3. We see the scaling law is roughly obeyed even for X_0 as high as 10^3. The increase in pressure at high densities is due to the thermalization of the fine-structure levels. Cooling then increases only linearly with density

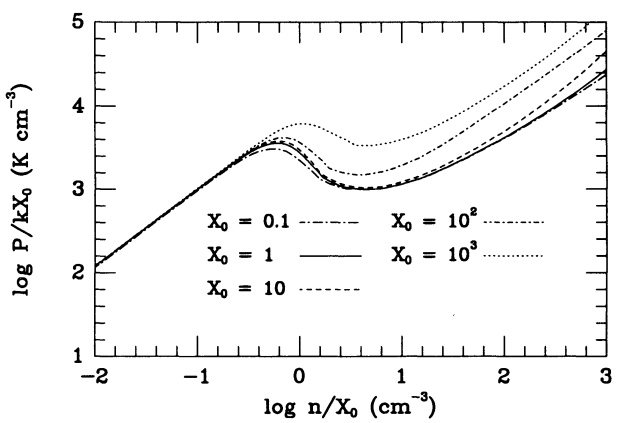

FIG. 8.—Thermal pressure P/kX_0 vs. hydrogen density n/X_0 for an absorbing column of $N_w = 10^{19}$ cm^{-2}. The parameter X_0 gives the common multiplier for G_0, ξ_{CR}, and the soft X-ray flux. Curves are shown for $X_0 = 0.1$ (*long dash-dot*), $X_0 = 1$ (*solid*), $X_0 = 10$ (*dash*), $X_0 = 10^2$ (*dash-dot*), and $X_0 = 10^3$ (*dot*).

$(n^2\Lambda \propto n)$, and thermal equilibrium requires higher temperatures. A result is that as X_0 increases, a two-phase medium is possible over a narrower range in pressures (see Table 3).

These results coupled with the metallicity dependence results of § 3.4 should be particularly significant for a theory of cloud formation as a function of Galactic radius, and in our understanding of the multiphase structure of high-velocity clouds in the Galactic halo. In addition, Figure 8 should be applicable to starburst galaxies in which values of $G_0 \gtrsim 10^3$ have been inferred from the fine-structure line emission (e.g., Wolfire, Tielens, & Hollenbach 1990; Carral et al. 1994) and where the supernova rates per unit volume are also $\sim 10^3$ times higher than the local Galactic ISM. In this subsection (and in § 3) we have illustrated the general trends in the pressure curve for simultaneous enhancements in the cosmic-ray flux and radiation field, and for lower metallicities. In a future paper we will apply these results to distant regions of the Galaxy and to extragalactic systems.

5. SUMMARY

We have calculated the thermal equilibrium gas temperature and constructed phase diagrams for the diffuse neutral interstellar medium. Our method uses results of BT to find the photoelectric heating from small grains and PAHs. The heating function accounts for the microphysics of particles extending into the molecular domain including a charge distribution for each particle size. In addition, we have explicitly included the heating and ionization due to the diffuse soft X-ray background and due to cosmic rays.

We find that under standard local conditions, photoelectric heating produces a stable two-phase medium with pressures in the range $P^{max}/k \simeq 3600$ K cm^{-3} to $P^{min}/k \simeq 990$ K cm^{-3}. The thermal instability between phases results from C II cooling which causes a rapid drop in temperature. For the parameter set $N_w = 10^{19}$ cm^{-2}, $G_0 = 1.7$ (average interstellar radiation field), $\mathscr{A}_C = 3.0 \times 10^{-4}$, and $\mathscr{A}_O = 4.6 \times 10^{-4}$, and at an equilibrium pressure of $P/k = 3000$ K cm^{-3}, we find a WNM with $T \simeq 7300$ K, $n \simeq 0.40$ cm^{-3}, and $n_e/n \simeq 2 \times 10^{-2}$, and a CNM with $T \simeq 45$ K, $n \simeq 60$ cm^{-3}, and $n_e/n \simeq 3 \times 10^{-4}$. The cooling by C II in each phase is given by $n\Lambda_{CII}^{CNM} \approx 6.2 \times 10^{-26}$ ergs s^{-1} H^{-1}, which accounts for $\sim 100\%$ of the cooling, and $n\Lambda_{CII}^{WNM} \approx 6.2 \times 10^{-27}$ ergs s^{-1} H^{-1}, which accounts for $\sim 25\%$ of the cooling. Between P^{min} and P^{max} the C II cooling ranges between 2.6 and 6.6×10^{-26} ergs s^{-1} H^{-1} in the CNM and $0.31–0.81 \times 10^{-26}$ ergs s^{-1} H^{-1} in the WNM. The calculated cooling rate for the CNM is in good agreement with observations (Pottasch et al. 1979; Gry et al. 1992). We conclude also that estimates of the energy input into the WNM based on C II alone can underestimate the total by a factor of $\sim 3–4$. These numbers for C II cooling in the disk can be reconciled with somewhat lower average C II cooling observed along lines of sight toward the Galactic halo (e.g., Bock et al. 1993; Savage et al. 1993) if we account for the reduced FUV field strength, lower pressures, and reduced columns of CNM toward these directions.

We have calculated the dependence of the thermal equilibrium results on the absorbing column density N_w, gas-phase and dust abundances, FUV field, and X-ray field. For $N_w \lesssim 10^{21}$ cm^{-2}, the dependence on N_w is caused by the attenuation of the diffuse X-ray flux. Increasing attenuation (increasing N_w) lowers the electron fraction, thereby increasing the positive grain charge and decreasing the grain photoelectric heating. For $N_w \gtrsim 3 \times 10^{19}$ cm^{-2}, the ionization by cosmic rays domi-

nates and the results are relatively independent of N_w until $N_w \gtrsim 10^{21}$ cm^{-2}, where dust attenuation of the FUV becomes significant. For $N_w < 3 \times 10^{19}$ cm^{-2}, the effect of the X-rays is to increase the range of pressures where two phases are possible.

Decreasing the gas-phase abundances of the coolants C and O raises the equilibrium gas temperatures and therefore raises the pressures where two phases are possible. Decreasing the dust abundance reduces the grain photoelectric heating and lowers the equilibrium gas temperatures and pressures. For dust abundances $\lesssim 0.03$ of the standard local interstellar values, the X-ray and cosmic-ray heating dominates and two phases are possible for 25 K cm$^{-3} \lesssim P/k \lesssim 250$ K cm^{-3}. Simultaneously decreasing the gas phase abundances of the coolants and the grain abundance by the same factor (as may occur in regions of low metallicity) results in a gradual increase in the pressures necessary for two-phase equilibrium, as X-ray heating becomes dominant (and constant) while cooling decreases.

The pressures necessary for two-phase equilibria rise as the FUV, X-ray, and cosmic-ray fluxes increase due to enhanced heating of the gas. If these three fluxes scale together with the common factor X_0, where $X_0 = 1$ is the local interstellar value, then the phase diagrams roughly obey a common scaling law when plotted as P/X_0 versus n/X_0 for $0.1 \leq X_0 \leq 1000$. However, the thermalization of the fine-structure levels at high density destroys the scaling with the result that as X_0 increases, a two-phase medium is possible over a narrow range in pressures. Likewise, if the FUV field rises alone, the pressures increase and the range of pressures necessary for two phases decreases until for $G_0 \gtrsim 10^2$ only one phase is stable. We have only studied $G_0 \lesssim 10^3$, but for $10^2 \leq G_0 \leq 10^3$, the WNM is stable for $P/k \gtrsim 10^5$ K cm^{-3} and the CNM is stable for larger pressures.

These results should be valuable in modeling the ISM in the Milky Way as a function of both galactocentric radius and height above the midplane. In addition, they will be useful in studies of the ISM near regions of massive star formation, such as in the nuclei of starburst galaxies. The most significant aspect, however, is the demonstration that a realistic and detailed model of grain photoelectric heating of the diffuse local ISM results in two stable phases which match observations without recourse to additional heat inputs.

We would like to thank John Raymond for the use of his plasma code, and for Dan McCammon for providing FORTRAN subroutines that calculate the X-ray opacity. M. G. W. was supported by the National Academy of Sciences through an NRC postdoctoral fellowship. Primary support for C. F. M. was provided from NSF grant AST 92-21289. Theoretical studies of interstellar dust at NASA Ames are supported under task 399-20-01-30 through NASA's Theory Program. This research was also supported in part by NASA RTOP 188-44-53 and by a special NASA Astrophysics Theory Program grant to the Center for Star Formation Studies at NASA Ames Research Center, the University of California at Berkeley, and the University of California at Santa Cruz.

APPENDIX A

IONIZATION AND HEATING BY SOFT X-RAYS

The functions $\phi^{\rm H}(E, n_e/n)$, and $\phi^{\rm He}(E, n_e/n)$ give the number of secondary ionizations of hydrogen and helium produced per primary electron. These functions depend on the primary electron energy E and electron fraction $x_e = n_e/n$. We use the coefficients listed in Table 2 of Shull & Van Steenberg (1985, hereafter SVS) to give the high-energy ($E \gg 100$ eV) dependence and fit their results shown in their Figure 3 for lower energies. We have

$$\phi^{\rm H}(E, x_e) = \left(\frac{E}{13.6} - 1\right) C(1 - x_e^a)^b \left(\frac{E}{1000}\right)^{cx_e} \quad \text{for} \quad E > 13.6 \text{ eV}, \tag{A1}$$

with $C = 0.3908$, $a = 0.4092$, $b = 1.7592$, from SVS, along with our fitted value for $c = 2.313$. This expression is usually good to $\pm 20\%$ for $E > 13.6$ eV and $3 \times 10^{-4} < x_e < 0.1$. However, for x_e greater than 3×10^{-2} and 28 eV $\lesssim E \lesssim 50$ eV the agreement drops to within $\pm 50\%$ while for $E \lesssim 28$ eV and $x_e > 3 \times 10^{-2}$ the function is good to within a factor of 2.

Assuming the energy dependence for He is similar to H we have

$$\phi^{\rm He}(E, x_e) = \left(\frac{E}{24.6} - 1\right) C(1 - x_e^a)^b \left(\frac{E}{1000}\right)^{cx_e} \quad \text{for} \quad E > 24.6 \text{ eV}, \tag{A2}$$

with $C = 0.0554$, $a = 0.4614$, $b = 1.6660$ from SVS, along with our value for $c = 2.313$ and similar error estimates as for H.

The function $E_h(E, n_e/n)$ gives the heat deposited for each primary electron of energy E. We use the coefficients given in SVS and Shull (1979) along with the functional form used by Binette, Dopita, & Tuohy (1985):

$$\frac{E_h(E, n_e/n)}{E} = f_1(x_e) + \left[\frac{f_2(E)}{f_3(x_e)} + \frac{1}{1 - f_1(x_e)}\right]^{-1}, \tag{A3}$$

where $f_1(x_e)$ determines the dependence on electron fraction at high energy

$$f_1(x_e) = C[1 - (1 - x_e^a)^b], \tag{A4}$$

with coefficients $C = 0.9971$, $a = 0.2663$, $b = 1.3163$ (SVS). The function $f_2(E)$ is given by

$$f_2(E) = 2E - 13.6 \text{ eV}, \tag{A5}$$

and the function $f_2(x_e)$ is a simple linear interpolation in $\log_{10}(x_e)$ to the values listed in Shull (1979); $f_3(10^{-4}) = 3.25$, $f_3(10^{-3}) = 7.20$, $f_3(10^{-2}) = 16.2$, and $f_3(10^{-1}) = 31.0$. The expression (A3) is good to $\pm 20\%$ for $E \gtrsim 28$ eV and $3 \times 10^{-4} < x_e < 0.1$.

The ionization and heating rates due to the soft X-ray background are illustrated in Figure 2 as functions of the (neutral) column N_w and ionization fraction in the gas, n_e/n. The X-ray radiation field is determined using the fit by Garmire et al. (1992) to the observed field. The calculations presented in this paper carry out the integrations of the X-ray radiation field over $\phi^{\rm H}(E, n_e/n)$, $\phi^{\rm He}(E, n_e/n)$, and $E_h(E, n_e/n)$ as indicated in equations (7) and (8). Here we provide simple analytic expressions for the resulting ionization and heating rates as functions of $p_1 = \log_{10}(N_w/10^{18}\ {\rm cm}^{-2})$, and $p_2 = \log_{10}(n_e/n)$. The ionization rate $\xi_{\rm XR}\ {\rm s}^{-1}$ is given by

$$\log_{10}(\xi_{\rm XR}) = f_4(p_2)(-15.6 - 1.10p_1 + 9.13 \times 10^{-2}p_1^2) + f_5(p_2)0.87 \exp\left[-\left(\frac{p_1 - 0.41}{0.84}\right)^2\right], \tag{A6}$$

where the functions f_4 and f_5 are given by

$$f_4(p_2) = 1.06 + 4.08 \times 10^{-2}p_2 + 6.51 \times 10^{-3}p_2^2, \tag{A7}$$

and

$$f_5(p_2) = 1.90 + 0.678p_2 + 0.113p_2^2, \tag{A8}$$

respectively. The fit for $\xi_{\rm XR}$ is good to $\pm 40\%$ for $18 < p_1 < 21$ and $-4 < p_2 < -1$.

The heating rate $\Gamma_{\rm XR}$ ergs s^{-1} is given by

$$\log_{10}(\Gamma_{\rm XR}) = f_6(p_2)(-26.5 - 0.920p_1 + 5.89 \times 10^{-2}p_1^2) + f_6(p_2)0.96 \exp\left[-\left(\frac{p_1 - 0.38}{0.87}\right)^2\right], \tag{A9}$$

where the function f_6 is

$$f_6(p_2) = 0.990 - 2.74 \times 10^{-3}p_2 + 1.13 \times 10^{-3}p_2^2. \tag{A10}$$

The fit for $\Gamma_{\rm XR}$ is good to $\pm 40\%$ for $18 < p_1 < 21$ and $-4 < p_2 < -0.3$.

APPENDIX B

C II COOLING

The cooling per hydrogen nucleus in the C II (158 μm) transition, for $n \ll n_{\rm cr} \approx 3 \times 10^3\ {\rm cm}^{-3}$, is given by

$$n\Lambda_{\rm C\,II} = 2.54 \times 10^{-14}\mathscr{A}_{\rm C} f_{\rm C\,II}[\gamma^{\rm H^0} n_{\rm H^0} + \gamma^e n_e] \exp(-92/T)\ {\rm ergs\ s^{-1}\ H^{-1}}, \tag{B1}$$

where $\gamma^{\rm H^0}$ and γ^e are the collisional de-excitation rate coefficients for collisions with neutral hydrogen and electrons, respectively, and $f_{\rm C\,II}$ is the fraction of C in C^+. We use the rates

$$\gamma^{\rm H^0} = 8.86 \times 10^{-10}\ {\rm cm^3\ s^{-1}}, \tag{B2}$$

and

$$\gamma^e = 2.1 \times 10^{-7}T_2^{-0.5}\Omega(T)\ {\rm cm^3\ s^{-1}}, \tag{B3}$$

where $T_n \equiv T/10^n$ K and the collision strength $\Omega(T)$ is given by

$$\Omega(T) = 1.80 + 0.484T_4 + 4.01T_4^2 - 3.39T_4^3 \tag{B4}$$

(see Table 1 for references).

The expression for the cooling rate simplifies in the WIM. Observations of diffuse ionized gas in the inner Galaxy indicate that the temperature of the WIM is in the range 3000–8000 K (Anantharamaiah 1985). Theoretical models of the local WIM suggest $T \sim 7500$ K (Mathis 1986), and we shall adopt this value for numerical estimates. Over the range 3000–8000 K, $\Omega(T) \simeq 3.27T_4^{0.32}$ to within 1%, where $T_4 = T/10^4$ K. The C II cooling function in the WIM then becomes

$$\Lambda_{\rm C\,II}^{\rm WIM} = 5.23 \times 10^{-25}\left(\frac{\mathscr{A}_{\rm C}}{3 \times 10^{-4}}\right) f_{\rm C\,II}\, x_e\, T_4^{-0.18}\ {\rm ergs\ cm^3\ s^{-1}}. \tag{B5}$$

If the WIM has a pressure $P = (1.1 + x_e)nkT$, the C II cooling rate per hydrogen nucleus is

$$n\Lambda_{\rm C\,II}^{\rm WIM} = 5.23 \times 10^{-26}(P/k)_3\left(\frac{\mathscr{A}_{\rm C}}{3 \times 10^{-4}}\right)\frac{x_e f_{\rm C\,II}}{1.1 + x_e}\, T_4^{-1.18}\ {\rm ergs\ s^{-1}\ H^{-1}}, \tag{B6}$$

where $(P/k)_3 = (P/k)/(10^3\ {\rm K\ cm^{-3}})$. For $x_e = 0.85$, $f_{\rm C\,II} = 0.85$, and $T_4 = 0.75$, this yields $n\Lambda_{\rm C\,II}^{\rm WIM} = 2.7 \times 10^{-26}(P/k)_3$ ergs s^{-1} H^{-1}.

For the particular case of a line of sight through the Galactic halo, the characteristic density in the WIM may be estimated from the Hα observations, which give an emission measure ${\rm EM} = 3.3T_4^{0.92}\ {\rm csc}\,|b|\ {\rm cm^{-6}\ pc}$ (Reynolds 1992), where b is Galactic latitude,

and from observations of pulsar dispersion measures, which indicate $N_e = 7 \times 10^{19} \csc|b| \text{ cm}^{-2}$ (Reynolds 1991a):

$$\langle n_e^{\rm WIM} \rangle^{\rm halo} = \frac{\int n_e^2 \, dl}{\int n_e \, dl} = 0.145 T_4^{0.92} \text{ cm}^{-3} . \quad \text{(B7)}$$

(The actual value of $\langle n_e^{\rm WIM} \rangle$ could be 10%–20% larger than this if electrons in the hot ionized medium make a significant contribution to the observed dispersion measures; Reynolds 1991b). This density corresponds to a halo pressure $P/k = 1900$ K cm^{-3}. Thus the cooling rate per hydrogen nucleus in the WIM along such a line of sight is

$$n^{\rm halo} \Lambda_{\rm C\,II}^{\rm WIM} = 7.58 \times 10^{-26} \left(\frac{\mathscr{A}_{\rm C}}{3 \times 10^{-4}} \right) f_{\rm C\,II} \, T_4^{0.74} \text{ ergs s}^{-1} \text{ H}^{-1} . \quad \text{(B8)}$$

REFERENCES

Allamandola, L. J., Tielens, A. G. G. M., & Barker, J. R. 1989, ApJS, 71, 733
Allen, C. W. 1976, Astrophysical Quantities (London: Athlone)
Anantharamaiah, K. R. 1985, J. Astrophys. Astron., 6, 203
Anders, E., & Grevesse, N. 1989, Geochim. Cosmochim. Acta, 53, 197
Bakes, E. L. O., & Tielens, A. G. G. M. 1994, ApJ, 427, 822 (BT)
Bałucińska-Church, M., & McCammon, D. 1992, ApJ, 400, 699
Barsuhn, J., & Walmsley, C. M. 1977, A&A, 54, 345
Begelman, M. C. 1990, in The Interstellar Medium in Galaxies, ed. H. A. Thronson, Jr., & J. M. Shull (Dordrecht: Kluwer), 287
Begelman, M. C., & McKee, C. F. 1990, ApJ, 358, 375
Binette, L., Dopita, M. A., & Tuohy, I. R. 1985, ApJ, 297, 476
Black, J. H., & van Dishoeck, E. F. 1987, ApJ, 322, 412
Black, J. H., van Dishoeck, E. F., Willner, S. P., & Woods, R. C. 1990, ApJ, 358, 459
Blandford, R. D., & Eichler, D. 1987, Phys. Rep., 154, 1
Blandford, R. D., & Ostriker, J. P. 1980, ApJ, 237, 793
Bock, J. J., et al. 1993, ApJ, 410, L115
Cardelli, J. A., Mathis, J. S., Ebbets, D. C., & Savage, B. D. 1993, ApJ, 402, L17
Carral, P., Hollenbach, D. J., Lord, S. D., Colgan, S. W. J., Haas, M. R., Rubin, R. H., & Erickson, E. F. 1994, ApJ, 423, 223
Chokshi, A., Tielens, A. G. G. M., Werner, M., & Castelaz, M. W. 1988, ApJ, 334, 803
Cunha, K., & Lambert, D. L. 1992, ApJ, 399, 586
Dalgarno, A., & McCray, R. A. 1972, ARA&A, 10, 375
de Jong, T. 1977, A&A, 55, 137
———. 1980, Highlights Astron., 5, 301
Dewar, R. L. 1970, Phys. Fluids, 11, 2710
d'Hendecourt, L., & Léger, A. 1987, A&A, 180, L9
Draine, B. T. 1978, ApJS, 36, 595
Draine, B. T., & Sutin, B. 1987, ApJ, 320, 803
Duley, W. W., & Williams, D. A. 1986, MNRAS, 219, 859
Edgar, R. J., Sanders, W. T., Juda, M., Kraushaar, W. L., & McCammon, D. 1993, BAAS, 25, 805
Federman, S. R., Glassgold, A. E., & Kwan, J. 1979, ApJ, 227, 466
Ferrière, K. M., Zweibel, E. G., & Shull, J. M. 1988, ApJ, 332, 984
Field, G. B. 1965, ApJ, 142, 531
Field, G. B., Goldsmith, D. W., & Habing, H. J. 1969, ApJ, 155, L149
Flower, D. 1990, Molecular Collisions in the Interstellar Medium (Cambridge: Cambridge Univ. Press), 61
Garmire, G. P., Nousek, J. A., Apparao, K. M. V., Burrows, D. N., Fink, R. L., & Kraft, R. P. 1992, ApJ, 399, 694
Giard, M., Lamarre, J. M., Pajot, F., & Serra, G. 1994, A&A, 286, 203
Glassgold, A. E., & Langer, W. D. 1974, ApJ, 193, 73
Gry, C., Lequeux, J., & Boulanger, F. 1992, A&A, 266, 457
Habing, H. J. 1968, Bull. Astron. Inst. Netherlands, 19, 421
Hayes, M. A., & Nussbaumer, H. 1984, A&A, 134, 193
Herbst, E. 1991, ApJ, 366, 133
Hollenbach, D., & McKee, C. F. 1989, ApJ, 342, 306 (HM)
Ip, W. H., & Axford, W. I. 1985, A&A, 149, 7
Jahoda, K., Lockman, F. J., & McCammon, D. 1990, ApJ, 354, 184
Jenkins, E. B. 1987, in Interstellar Processes, ed. D. Hollenbach & H. A. Thronson, Jr. (Dordrecht: Reidel), 533
Jenkins, E. B., Jura, M., & Loewenstein, M. 1983, ApJ, 270, 88
Jenkins, E. B., & Shaya, E. J. 1979, ApJ, 231, 55
Jones, A. P., Tielens, A. G. G. M., Hollenbach, D., & McKee, C. F. 1994, ApJ, 433, 797
Jura, M. 1976, ApJ, 204, 12
Keller, R. 1987, in PAHs and Astrophysics, ed. A. Léger, L. d'Hendecourt, & N. Boccara (Dordrecht: Reidel), 387
Kulkarni, S. R., & Fich, M. 1985, ApJ, 289, 792
Kulkarni, S. R., & Heiles, C. 1987, in Interstellar Processes, ed. D. Hollenbach & H. A. Thronson, Jr. (Dordrecht: Reidel), 87
Kulkarni, S. R., & Heiles, C. 1988, in Galactic and Extragalactic Radio Astronomy, ed. G. L. Verschuur & K. I. Kellermann (New York: Springer), 95
Launay, J.-M., & Roueff, E. 1977, J. Phys. B., 10, 879
Lazareff, B. 1975, A&A, 42, 225
Lepp, S., & Dalgarno, A. 1988, ApJ, 335, 769
Mathis, J. S. 1986, ApJ, 301, 423
Mathis, J. S., Rumpl, W., & Nordsieck, K. H. 1977, ApJ, 217, 425 (MRN)
McCammon, D., & Sanders, W. T. 1990, ARA&A, 28, 657
McKee, C. F. 1994, in preparation
McKee, C. F., & Ostriker, J. P. 1977, ApJ, 218, 148 (MO)
Mebold, U. 1972, A&A, 19, 13
Mebold, U., Winnberg, A., Kalberla, P. M. W., & Goss, W. M. 1982, A&A, 115, 223
Omont, A. 1986, A&A, 164, 159
Osterbrock, D. E. 1989, Astrophysics of Gaseous Nebulae and Active Galactic Nuclei (Mill Valley: University Science)
Payne, H. E., Salpeter, E. E., & Terzian, Y. 1983, ApJ, 272, 540
Péquignot, D. 1990, A&A, 231, 499
Pottasch, S. R., Wesselius, P. R., & van Duinen, R. J. 1979, A&A, 74, L15
Puget, J. L., & Léger, A. 1989, ARA&A, 27, 161
Puget, J. L., Léger, A., & Boulanger, F. 1985, A&A, 142, L19
Raymond, J. C., & Smith, B. W. 1977, ApJS, 35, 419
———. 1993, private communication
Reynolds, R. J. 1991a, in The Interstellar Disk Halo Connection in Galaxies, ed. H. Bloemen (Dordrecht: Kluwer), 67
———. 1991b, ApJ, 372, L17
———. 1992, ApJ 392, L35
Rubin, R. H., Dufour, R. J., & Walter, D. K. 1993, ApJ, 413, 242
Sanders, W. T., Edgar, R. J., Juda, M., Kraushaar, W. L., & McCammon, D. 1993, BAAS, 25, 804
Savage, B. D., Lu, L., Weyman, R. J., Morris, S. L., & Gilliland, R. L. 1993, ApJ, 404, 124
Shull, J. M. 1979, ApJ, 234, 761
———. 1987, in Interstellar Processes, ed. D. Hollenbach & H. A. Thronson, Jr. (Dordrecht: Reidel), 225
Shull, J. M., & Van Steenberg, M. E. 1985, ApJ, 298, 268 (SVS)
Shull, J. M., & Woods, D. T. 1985, ApJ, 288, 50
Silk, J., & Werner, M. 1969, ApJ, 158, 185
Spitzer, L. 1978, Physical Processes in the Interstellar Medium (New York: Wiley)
———. 1990, ARA&A, 28, 71
Spitzer, L., & Fitzpatrick, E. L. 1993, ApJ, 409, 299
Spitzer, L., & Jenkins, E. B. 1975, ARA&A, 13, 133
Sutherland, R. S., & Shull, J. M. 1994, BAAS, 25, 1312
Tielens, A. G. G. M. 1993, in Dust and Chemistry in Astronomy, ed. T. J. Millar & D. H. Williams (Bristol: Institute of Physics Publishing), 103
Tielens, A. G. G. M., & Allamandola, L. J. 1987, in Physical Processes in Interstellar Clouds, ed. G. Morfill & M. Scholer (Dordrecht: Reidel), 333
Tielens, A. G. G. M., & Hollenbach, D. 1985a, ApJ, 291, 722
———. 1985b, ApJ, 291, 747
Van Dishoeck, E. F., & Black, J. H. 1986, ApJS, 64, 109
Van Steenberg, M. E., & Shull, J. M. 1988, ApJ, 330, 942
Verstraete, L., Léger, A., d'Hendecourt, L., Dutuit, O., & Défourneau, D. 1990, A&A, 237, 436
Walter, D. K., Dufour, R. J., & Hester, J. J. 1992, ApJ, 397, 196
Watson, W. D. 1972, ApJ, 176, 103
Werner, M. W., Silk, J., & Rees, M. J. 1970, ApJ, 161, 965
Wolfire, M. G., & Königl, A. 1991, ApJ, 383, 205
Wolfire, M. G., Tielens, A. G. G. M., & Hollenbach, D. 1990, ApJ, 358, 116
Wright, E. L., et al. 1991, ApJ, 381, 200
York, D. G., & Frisch, P. 1984, in IAU Colloq. 81, Local Insterstellar Medium, ed. Y. Kondo, F. C. Bruhweiler, & B. D. Savage (NASA CP-2345), 51